

Fractional Maps as Maps with Power-Law Memory

Mark Edelman

Abstract The study of systems with memory requires methods which are different from the methods used in regular dynamics. Systems with power-law memory in many cases can be described by fractional differential equations, which are integro-differential equations. To study the general properties of nonlinear fractional dynamical systems we use fractional maps, which are discrete nonlinear systems with power-law memory derived from fractional differential equations. To study fractional maps we use the notion of α -families of maps depending on a single parameter $\alpha > 0$ which is the order of the fractional derivative in a nonlinear fractional differential equation describing a system experiencing periodic kicks. α -families of maps represent a very general form of multi-dimensional nonlinear maps with power-law memory, in which the weight of the previous state at time t_i in defining the present state at time t is proportional to $(t - t_i)^{\alpha-1}$. They may be applicable to studying some systems with memory such as viscoelastic materials, electromagnetic fields in dielectric media, Hamiltonian systems, adaptation in biological systems, human memory, etc. Using the fractional logistic and standard α -families of maps as examples we demonstrate that the phase space of nonlinear fractional dynamical systems may contain periodic sinks, attracting slow diverging trajectories, attracting accelerator mode trajectories, chaotic attractors, and cascade of bifurcations type trajectories whose properties are different from properties of attractors in regular dynamical systems.

Mark Edelman
Stern College at Yeshiva University, 245 Lexington Street, New York, NY 10016 and
Courant Institute of Mathematical Sciences at NYU, New York, NY 10012
e-mail: edelman@cims.nyu.edu

1 Introduction

Many natural and social systems are systems with memory. Their mathematical description requires solving integro-differential equations and is quite complicated. Maps with memory are used to model real systems with memory in order to derive their basic properties.

1.1 Systems with Memory

Writing this text I am recalling the content of my latest papers. It is easy to recall the content of my last paper but it becomes more and more difficult as I try to recall papers that are more and more distant in time. Memory is a significant property of human beings and is the subject of extensive biophysical and psychological research. As it has been demonstrated in experiments, forgetting - the accuracy on a memory tasks decays as a power law, $\sim t^{-\beta}$, with $0 < \beta < 1$ [37, 66, 87, 88, 89]. It is interesting that fractional maps corresponding to fractional differential equations of the order $0 < \alpha < 1$ are maps with the power-law decaying memory in which the power is $-\beta = \alpha - 1$ and $0 < \beta < 1$ [20]. Human learning is closely related to memory. It also can be described by a power law: the reduction in reaction times that comes with practice is a power function of the number of training trials [1]. There are multiple publications where power-law adaptation has been applied in describing the dynamics of biological systems at levels ranging from single ion channels up to human psychophysics [23, 43, 82, 83, 89, 96].

Power-law memory applies not only to the human being as a whole, but also to the hierarchy of its building blocks, from individual neurons and proteins to the tissue of individual organs. It has been shown recently [47, 48] that processing of external stimuli by individual neurons can be described by fractional differentiation. The orders of fractional derivatives α derived for different types of neurons fall within the interval $[0, 1]$. For neocortical pyramidal neurons it is quite small: $\alpha \approx 0.15$. Fluctuations within single protein molecules demonstrate a power-law memory kernel with the exponent -0.51 ± 0.07 [57].

Viscoelastic properties of human tissues were demonstrated in many examples: the brain and the central nervous system in general [10, 44, 49], the breast [12], the liver [41, 81], the spleen [61], the prostate [36, 95], the arteries [13, 14], the muscles [31] (see also references for some other human and animal organs tissues [16, 50, 55, 60, 69]). Viscoelastic materials obey the following stress-strain relationship:

$$\sigma(t) = E(\gamma) \frac{d^\alpha \gamma(t)}{dt^\alpha}, \quad (1)$$

where σ is the stress, γ is the strain, α is the order of the fractional derivative, and t is time. In most of the cases for human tissues $0 < \alpha < 1$ and is close to zero. In some cases, e.g. for modeling of the accurate placement of the needle tip into

the target tissue during needle insertion treatments for liver tumors, nonlinearity of $E(\gamma)$ should be taken into account [41]. In the last example a simple quadratic nonlinearity and $\alpha = 0.1$ were used.

A Fourier transform of a fractional derivative is [40, 63, 67]

$$F\{D^\alpha g(t); \omega\} = (-i\omega)^\alpha \hat{g}(\omega), \quad (2)$$

where $\hat{g}(\omega) = F\{g(t); \omega\}$. As a result, whenever the term $(\omega)^\alpha \hat{g}(\omega)$ appears in the frequency domain, there is a good chance that function $g(t)$ is a solution of a fractional differential equation with a fractional derivative of the order α and the corresponding system is a system with power-law memory. Well known examples of such systems are dielectrics. Electromagnetic fields in dielectric media are described by equations with time fractional derivatives due to the 'universal' response - the power-law frequency dependence of the dielectric susceptibility in a wide range of frequencies [73, 74, 77, 78]. Similarly, elastic wave attenuation in biological tissue over a wide range of frequencies follows the power law $\alpha(\omega) \propto \omega^\eta$ with $\eta \in [0, 2]$ [17, 34, 59, 71] which implies a fractional wave equation. The establishment of accurate fractional wave-propagation models is important for many medical applications [59].

Above we concentrated on biological systems with memory in order to emphasize the importance of the study of nonlinear fractional dynamical systems described by fractional differential equations of the order $0 < \alpha < 2$ and especially α close to zero which is a major subject of the following sections (Sec. 3.2 and 3.3). Now we'll list some (not all) other examples of systems with power-law memory. As has been mentioned above, time fractional derivatives and correspondingly systems with power-law memory in many cases are used to describe viscoelasticity and rheology (for the original papers and reviews see [4, 5, 8, 9, 51, 52, 53, 54], for nonlinear effects see [64, 65, 85, 86]). Electromagnetic fields in dielectric media were also mentioned above. Hamiltonian systems and billiards are also systems with power-law memory, in which the fractal structure of the phase space and stickiness of trajectories in time imply description of transport by the fractional (fractional time and space derivatives) Fokker-Plank-Kolmogorov equation [90, 91, 92, 93]. In some cases [38, 39, 40] fractional differential equations are equivalent to the Volterra integral equations of the second kind. Systems considered in population biology and epidemiology are systems with memory and Volterra integral equations are frequently used to describe such systems [6, 35]. Long-term memory provides more robust control in linear and nonlinear control theory (see books [7, 62]).

1.2 Maps with Memory

As in the study of regular dynamics, in the study of systems with memory use of discrete maps significantly simplifies investigation of the general properties of the corresponding systems. In some cases of kicked systems maps are equivalent to the

original differential equations. Historically, maps with memory were first considered as analogues of the integro-differential equations of non-equilibrium statistical physics [26, 27, 32], with regards to thermodynamic theory of systems with memory [30], and to model non-Markovian processes in general [28, 29]. The most general form of a map with memory is

$$\mathbf{x}_{n+1} = \mathbf{f}_{n+1}(\mathbf{x}_n, \mathbf{x}_{n-1}, \dots, \mathbf{x}_0, P), \quad (3)$$

where \mathbf{x}_k are N -dimensional vectors, $k, N \in \mathbb{Z}$, $k \geq 0$, and P is a set of parameters. It is almost impossible to derive the general properties of systems with memory from Eq. (3) and simplified forms of maps with memory are used. The most commonly used form is the one-dimensional map with long-term memory

$$x_{n+1} = \sum_{k=0}^n V_\alpha(n, k) G_K(x_k), \quad (4)$$

where $V_\alpha(n, k)$ and α characterize memory effects and K is a parameter. In many cases weights are taken as convolutions with $V_\alpha(n, k) = V_\alpha(n - k)$. The particular form of Eq. (4) with constant weights

$$x_{n+1} = c \sum_{k=0}^n G_K(x_k) \quad (5)$$

is called a full-memory map. It is easy to note that Eq. (5) is equivalent to

$$x_{n+1} = x_n + c G_K(x_n), \quad (6)$$

which means that maps with full memory are maps with one-step memory in which all memory is accumulated in the present state of a system and the next values of map variables are fully defined by their present values. We won't consider maps with short memory in which the number of terms in the sum in Eq. (4) is bounded (from $k = n - M + 1$ to $k = n$).

Initial investigations of long-term memory maps were done mostly on different modifications of the logistic map and exponential memory. The general applicability of their results to systems with memory in general is limited. Recently Stanislavsky [70] considered the maps Eq. (4) with $G_K(x) = Kx(1 - x)$ (the logistic map) and the weights $V_\alpha(n, k)$ as a combination of power-law functions taken from one of algorithms of numerical fractional integration. He came to the conclusion that increase in long-term memory effects leads to a less chaotic behavior.

First maps with power-law memory equivalent to fractional differential equations were derived in [75, 76, 78, 79, 80] by integrating fractional differential equations describing systems under periodic kicks. The method used is similar to the way in which the universal map is derived in regular dynamics.

1.3 Universal Map

In the following section (Sec. 2) we will modify the way presented in Sec. 1.3 to derive the universal map in regular dynamics (see [11], and Ch. 5 from [90]) in order to derive the universal fractional map.

The universal map can be derived from the differential equation

$$\ddot{x} + KG(x) \sum_{n=-\infty}^{\infty} \delta\left(\frac{t}{T} - (n + \varepsilon)\right) = 0, \quad (7)$$

where $0 < \varepsilon < 1$ and K is a parameter, with the initial conditions:

$$x(0) = x_0, \quad p(0) = \dot{x}(0) = p_0. \quad (8)$$

This equation is equivalent to the Volterra integral equation of second kind

$$x(t) = x_0 + p_0 t - K \int_0^t d\tau G(x(\tau)) \sum_{n=-\infty}^{\infty} \delta\left(\frac{\tau}{T} - (n + \varepsilon)\right) (t - \tau). \quad (9)$$

Eq. (9) for $(n + \varepsilon)T < t < (n + 1 + \varepsilon)T$ has a solution

$$\begin{aligned} x(t) &= x_0 + p_0 t - KT \sum_{k=0}^n G(x(Tk + T\varepsilon))(t - Tk - T\varepsilon), \\ p(t) = \dot{x}(t) &= p_0 - KT \sum_{k=0}^n G(x(Tk + T\varepsilon)). \end{aligned} \quad (10)$$

After the introduction of the map variables

$$x_n = x(Tn), \quad p_n = p(Tn) \quad (11)$$

Eq. (10) considered for time instances $t=(n+1)T$ gives

$$\begin{aligned} x_{n+1} &= x_0 + p_0(n+1)T - KT^2 \sum_{k=0}^n G(x(Tk + T\varepsilon))(n - k + 1 - \varepsilon), \\ p_{n+1} &= p_0 - KT \sum_{k=0}^n G(x(Tk + T\varepsilon)). \end{aligned} \quad (12)$$

As it follows from Eq. (10), $\dot{x}(t) = p(t)$ is a bounded function with the discontinuities at the time instances of the kicks (at $t = Tk + T\varepsilon$) and $x(t)$ is a continuous function. This allows us to calculate $G(x)$ at the time instances of the kicks. In the limit $\varepsilon \rightarrow 0$ Eq. (12) gives

$$\begin{aligned}
x_{n+1} &= x_0 + p_0(n+1)T - KT^2 \sum_{k=0}^n G(x_k)(n-k+1), \\
p_{n+1} &= p_0 - KT \sum_{k=0}^n G(x_k).
\end{aligned} \tag{13}$$

Eq. (13) is a form of the universal map which allows further simplifications. It can be written in a symmetric form as a map with full memory (see Sec. 1.2):

$$\begin{aligned}
x_{n+1} &= x_0 + T \sum_{k=1}^{n+1} p_k, \\
p_{n+1} &= p_0 - KT \sum_{k=0}^n G(x_k).
\end{aligned} \tag{14}$$

As we saw in Sec. 1.2, maps with full memory are equivalent to maps with one-step memory. Map Eq. (14) can be written as the iterative area preserving $(\partial(p_{n+1}, x_{n+1})/\partial(p_n, x_n) = 1)$ process with one-step memory which is called the universal map:

$$p_{n+1} = p_n - KTG(x_n), \tag{15}$$

$$x_{n+1} = x_n + p_{n+1}T. \tag{16}$$

This map represents the relationship between the values of the physical variables in Eq. (7) on the left sides of the consecutive kicks. The standard map may be obtained from the universal map by assuming $G(x) = \sin(x)$:

$$\begin{aligned}
p_{n+1} &= p_n - K \sin x, \quad (\text{mod } 2\pi), \\
x_{n+1} &= x_n + p_{n+1}, \quad (\text{mod } 2\pi).
\end{aligned} \tag{17}$$

Here we assumed $T = 1$ and consider this map on a torus (mod 2π).

Derivation of the fractional universal map in the next section (Sec. 2) follows [20] and the analysis of this map for $\alpha \in (0, 1)$ and $\alpha \in (1, 2)$ in Secs. 3.2 and 3.3 follows [19, 20, 21, 22].

2 Fractional Universal Map

The one-dimensional logistic map

$$x_{n+1} = Kx_n(1 - x_n) \tag{18}$$

may be presented in the 2D form

$$\begin{aligned}
p_{n+1} &= -G_{IK}(x_n), \\
x_{n+1} &= x_n + p_{n+1},
\end{aligned} \tag{19}$$

where

$$G_{IK}(x) = x - Kx(1 - x). \quad (20)$$

It can't be written as a particular form of the universal map Eqs. (15) and (16). In order to derive the logistic map from the universal map we'll introduce the notion of the n-dimensional universal map depending on a single parameter.

2.1 Universal Integer-Dimensional Maps

Solution of the one-dimensional analog of Eq. (7) would require calculations of the function $G(x)$ at the time instances of the kicks $T(n + \varepsilon)$ at which $x(t)$ is discontinuous. To enable us to introduce the universal fractional map we'll include a time delay ΔT into the argument of the function $G(x(t))$ (see Fig. 1). In order to extend the class of maps which are particular forms of the universal map we'll also consider K not as a factor but as a parameter. Let's consider the following generating equation:

$$\dot{x} + G_K(x(t - \Delta T)) \sum_{n=-\infty}^{\infty} \delta\left(\frac{t}{T} - (n + \varepsilon)\right) = 0, \quad (21)$$

where $0 < \varepsilon < 1$ and $0 < \Delta < 1$ with the initial condition:

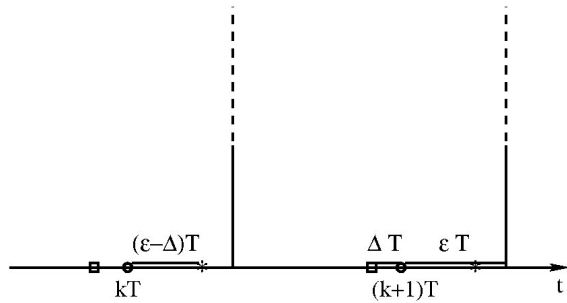
$$x(0) = x_0. \quad (22)$$

1D analog of Eq. (10) (for $(n + \varepsilon)T < t < (n + 1 + \varepsilon)T$) can be written as

$$x(t) = x_0 - T \sum_{k=0}^n G_K(x[T(k + \varepsilon - \Delta)]). \quad (23)$$

From the fact that $\dot{x} = 0$ for $t \in (T(k + \varepsilon - 1), T(k + \varepsilon))$ it follows that $x[T(k + \varepsilon - \Delta)] = x(Tk)$ and the corresponding 1D map can be written as a map with full memory

Fig. 1 The universal map is a relationship between values of $x(t)$ considered at the times kT (small circles). The kicks occur at the time instances $(k + \varepsilon)T$ (vertical lines). With the time delay ΔT (distance between the squares and the circles) the function $G_K(x(t))$ is calculated at the time instances $t = (k + \varepsilon - \Delta)T$ (stars).



$$x_{n+1} = x_0 - T \sum_{k=0}^n G_K(x_k). \quad (24)$$

From Sec. 1.2 it follows that this map can be written as the 1D form of the universal map with one-step memory

$$x_{n+1} = x_n - T G_K(x_n). \quad (25)$$

It would be impossible to derive the logistic map from Eq. (25) if K were a factor, but from the present form the logistic map can be obtained by assuming

$$G_K(x) = G_{IK}(x) = \frac{1}{T} [x - Kx(1-x)]. \quad (26)$$

In [6, 72] Eq. (21) with no time delay, no delta functions, and $G_K(x)$ defined by Eq. (26) is used as one of the most general models in population biology and epidemiology. Three terms in $G_K(x)$ represent a growth rate proportional to the current population, restrictions due to the limited resources, and the death rate. The logistic map appears and plays an important role not only in population biology but also in economics, condensed matter physics, and other areas of science [3, 72]. In population biology and epidemiology time delays can be related to the time of the development of an infection in a body until a person becomes infectious, or to the time of the development of an embryo. For the importance of time delay in many scientific applications of the logistic map see e.g. Ch. 3 from [72] and Ch. 3 from [3]. Changes which occur as periodically following discrete events can be modeled by the delta function.

The n-dimensional universal map can be derived from the following generating equation:

$$\frac{d^n x}{dt^n} + G_K(x(t-\Delta)) \sum_{k=-\infty}^{\infty} \delta(t - (k + \varepsilon)) = 0, \quad (27)$$

where $n \geq 0$, $n \in \mathbb{Z}$, and $\varepsilon > \Delta > 0$ in the limit $\varepsilon \rightarrow 0$. This means that in the general case time delay is not essential. Without losing the generality, in Eq. (27) we assumed $T = 1$. The case $T \neq 1$ is considered in [20] and can be reduced to this case by rescaling the time variable and the map generating function $G_K(x)$. In Sec. 3 T denotes periods of trajectories. The 2D universal map Eqs. (15) and (16) corresponds to $n = 2$ and the 1D universal map (25) corresponds to $n = 1$. In the consistent introduction of fractional derivatives integer derivatives appear as the limits when the order of a fractional derivative assumes an integer value. Correspondingly, the general form of the n-dimensional universal map appears if we assume an integer value of α in the general form of the fractional universal map. In the following sections we'll consider the general forms of the fractional universal map which will be derived from Eq. (27) with integer n replaced by $\alpha \in \mathbb{R}$ ($\alpha \geq 0$). The Riemann-Liouville universal map will be derived in Sec. 2.2 and the Caputo universal map will be derived in Sec. 2.3.

2.2 Riemann-Liouville Universal Map

The generating fractional differential equation for the Riemann-Liouville universal map can be written as

$${}_0D_t^\alpha x(t) + G_K(x(t-\Delta)) \sum_{n=-\infty}^{\infty} \delta(t - (n + \varepsilon)) = 0, \quad (28)$$

where $\varepsilon > \Delta > 0$, $\varepsilon \rightarrow 0$, $0 \leq N-1 < \alpha \leq N$, $\alpha \in \mathbb{R}$, $N \in \mathbb{Z}$, and the initial conditions

$$({}_0D_t^{\alpha-k} x)(0+) = c_k, \quad k = 1, \dots, N. \quad (29)$$

The left-sided Riemann-Liouville fractional derivative ${}_0D_t^\alpha x(t)$ is defined for $t > 0$ [40, 63, 67] as

$${}_0D_t^\alpha x(t) = D_t^n {}_0I_t^{n-\alpha} x(t) = \frac{1}{\Gamma(n-\alpha)} \frac{d^n}{dt^n} \int_0^t \frac{x(\tau) d\tau}{(t-\tau)^{\alpha-n+1}}, \quad (30)$$

where $n-1 \leq \alpha < n$, $D_t^n = d^n/dt^n$, and ${}_0I_t^\alpha$ is a fractional integral.

For a wide class of functions $G_K(x)$ Eq. (28) is equivalent to the Volterra integral equation of the second kind ($t > 0$) (see [38, 39, 40, 78])

$$x(t) = \sum_{k=1}^N \frac{c_k}{\Gamma(\alpha-k+1)} t^{\alpha-k} - \frac{1}{\Gamma(\alpha)} \int_0^t d\tau \frac{G_K(x(\tau-\Delta))}{(t-\tau)^{1-\alpha}} \sum_{k=-\infty}^{\infty} \delta(\tau - (k + \varepsilon)). \quad (31)$$

Due to the presence of the delta function the integral on the right side of Eq. (31) can be easily calculated [20, 75, 76, 78] for $t > 0$:

$$x(t) = \sum_{k=1}^{N-1} \frac{c_k}{\Gamma(\alpha-k+1)} t^{\alpha-k} - \frac{1}{\Gamma(\alpha)} \sum_{k=0}^{[t-\varepsilon]} \frac{G_K(x(k+\varepsilon-\Delta))}{(t-(k+\varepsilon))^{1-\alpha}} \Theta(t - (k + \varepsilon)), \quad (32)$$

where $\Theta(t)$ is the Heaviside step function. In Eq. (32) we took into account that boundedness of $x(t)$ at $t = 0$ requires $c_N = 0$ and $x(0) = 0$. After the introduction (see [80])

$$p(t) = {}_0D_t^{\alpha-N+1} x(t) \quad (33)$$

and

$$p^{(s)}(t) = D_t^s p(t), \quad (34)$$

where $s = 0, 1, \dots, N-2$, Eq. (32) leads to

$$\begin{aligned}
p^{(s)}(t) &= \sum_{k=1}^{N-s-1} \frac{c_k}{(N-s-1-k)!} t^{N-s-1-k} \\
&- \frac{1}{(N-s-2)!} \sum_{k=0}^{\lfloor t-\varepsilon \rfloor} G_K(x(k+\varepsilon-\Delta))(t-k)^{N-s-2}, \quad (35)
\end{aligned}$$

where $s = 0, 1, \dots, N-2$. Assuming $x_n = x(n)$, for $\varepsilon > \Delta > 0$ Eqs. (32) and (35) in the limit $\varepsilon \rightarrow 0$ give the equations of the Riemann-Liouville universal map

$$\begin{aligned}
x_{n+1} &= \sum_{k=1}^{N-1} \frac{c_k}{\Gamma(\alpha-k+1)} (n+1)^{\alpha-k} \\
&- \frac{1}{\Gamma(\alpha)} \sum_{k=0}^n G_K(x_k)(n-k+1)^{\alpha-1}, \quad (36)
\end{aligned}$$

$$\begin{aligned}
p_{n+1}^s &= \sum_{k=1}^{N-s-1} \frac{c_k}{(N-s-1-k)!} (n+1)^{N-s-1-k} \\
&- \frac{1}{(N-s-2)!} \sum_{k=0}^n G_K(x_k)(n-k+1)^{N-s-2}. \quad (37)
\end{aligned}$$

2.3 Caputo Universal Map

Similar to (28), the generating fractional differential equation for the Caputo universal map can be written as

$${}_0^C D_t^\alpha x(t) + G_K(x(t-\Delta)) \sum_{n=-\infty}^{\infty} \delta(t-(n+\varepsilon)) = 0, \quad (38)$$

where $\varepsilon > \Delta > 0$, $\varepsilon \rightarrow 0$, $0 \leq N-1 < \alpha \leq N$, $\alpha \in \mathbb{R}$, $N \in \mathbb{Z}$, and the initial conditions

$$(D_t^k x)(0+) = b_k, \quad k = 0, \dots, N-1. \quad (39)$$

The left-sided Caputo fractional derivative ${}_0^C D_t^\alpha x(t)$ is defined for $t > 0$ [40, 63, 67] as

$${}_0^C D_t^\alpha x(t) = {}_0 I_t^{n-\alpha} D_t^n x(t) = \frac{1}{\Gamma(n-\alpha)} \int_0^t \frac{D_\tau^n x(\tau) d\tau}{(t-\tau)^{\alpha-n+1}}, \quad (40)$$

where $n-1 < \alpha \leq n$.

For a wide class of functions $G_K(x)$ Eq. (38) is equivalent to the Volterra integral equation of the second kind ($t > 0$) (see [38, 39, 40, 78])

$$x(t) = \sum_{k=0}^{N-1} \frac{b_k}{k!} t^k - \frac{1}{\Gamma(\alpha)} \int_0^t d\tau \frac{G_K(x(\tau-\Delta))}{(t-\tau)^{1-\alpha}} \sum_{k=-\infty}^{\infty} \delta(\tau-(k+\varepsilon)). \quad (41)$$

Integration of this equation gives for $t > 0$

$$x(t) = \sum_{k=0}^{N-1} \frac{b_k}{k!} t^k - \frac{1}{\Gamma(\alpha)} \sum_{k=0}^{\lceil t-\varepsilon \rceil} \frac{G_K(x(k+\varepsilon-\Delta))}{(t-(k+\varepsilon))^{1-\alpha}} \Theta(t-(k+\varepsilon)). \quad (42)$$

After the introduction $x^{(s)}(t) = D_t^\alpha x(t)$ the Caputo universal map can be derived in the form (see [78])

$$x_{n+1}^{(s)} = \sum_{k=0}^{N-s-1} \frac{x_0^{(k+s)}}{k!} (n+1)^k - \frac{1}{\Gamma(\alpha-s)} \sum_{k=0}^n G_K(x_k) (n-k+1)^{\alpha-s-1}, \quad (43)$$

where $s = 0, 1, \dots, N-1$.

3 α -Families of Maps

We'll call Eqs. (28) and (29) with various map generating functions $G_K(x)$ the Riemann-Liouville universal map generating equations and Eqs. (36) and (37) the Riemann-Liouville α -families of maps corresponding to the functions $G_K(x)$. We'll call Eqs. (38) and (39) with various map generating functions $G_K(x)$ the Caputo universal map generating equations and Eqs. (43) the Caputo α -families of maps corresponding to the functions $G_K(x)$.

Fractional maps Eqs. (36), (37), and (43) are maps with memory in which the next values of map variables depend on all previous values. An increase in α corresponds to the increase in a map dimension. It also corresponds to the increased power in the power-law dependence of weights of previous states which imply increased memory effects. For $\alpha = 1$ and $\alpha = 2$ the corresponding maps are given by Eqs. (25), (15), and (16) with $T = 1$ and $G_K(x)$ instead of $G(x)$. Eqs. (36), (37), and (43) with $\alpha = 3$ and variables $y = p$ and $z = \dot{p}$ produce the full-memory 3D Universal Map

$$\begin{aligned} x_{n+1} &= \frac{z_0}{2}(n+1)^2 + y_0(n+1) + x_0 - \frac{1}{2} \sum_{k=0}^n G_K(x_k) (n-k+1)^2, \\ y_{n+1} &= z_0(n+1) + y_0 - \sum_{k=0}^n G_K(x_k) (n-k+1), \\ z_{n+1} &= z_0 - \sum_{k=0}^n G_K(x_k), \end{aligned} \quad (44)$$

which is equivalent to the one-step memory (Sec. 1.2) 3D universal map

$$\begin{aligned}
x_{n+1} &= x_n - \frac{1}{2}G_K(x_n) + y_n + \frac{1}{2}z_n, \\
y_{n+1} &= -G_K(x_n) + y_n + z_n, \\
z_{n+1} &= -G_K(x_n) + z_n,
\end{aligned} \tag{45}$$

or

$$\begin{aligned}
x_{n+1} &= x_n + y_{n+1} - \frac{1}{2}z_{n+1}, \\
y_{n+1} &= y_n + z_{n+1}, \\
z_{n+1} &= -G_K(x_n) + z_n,
\end{aligned} \tag{46}$$

which is a volume preserving map. This map has fixed points $z_0 = y_0 = G_K(x_0) = 0$ and stability of these points can be analyzed by considering the eigenvalues λ of the matrix (corresponding to the tangent map)

$$\begin{pmatrix} 1 - 0.5\dot{G}_K(x_0) & 1 & 0.5 \\ -\dot{G}_K(x_0) & 1 & 1 \\ -\dot{G}_K(x_0) & 0 & 1 \end{pmatrix}.$$

The only case in which the fixed points could be stable is $\dot{G}_K(x_0) = 0$, when $\lambda_1 = \lambda_2 = \lambda_3 = 1$. From Eq. (46) it follows that the only $T = 2$ points are the fixed points.

The investigation of the integer members of the α -families of maps is a subject of ongoing research. From the examples of maps with the values of α equal to one, two, and three we see that integer values of α correspond to the degenerate cases in which map equations can be written as maps with full memory. They are equivalent to α -dimensional one-step memory maps in which map variables at each step accumulate information about all previous states of the corresponding systems.

Corresponding to the fact that in the $\alpha = 2$ case the 2D universal family of maps produces the standard map if $G_K(x) = K \sin(x)$ (see Eqs. (17)) and in the $\alpha = 1$ case the logistic map results from $G_K(x) = x - Kx(1-x)$ (see Eqs. (25) and (26)), we'll call:

- the Riemann-Liouville α -family of maps Eqs. (36) and (37) with $G_K(x) = K \sin(x)$ the **standard α -RL-family of maps**;
- the Caputo α -family of maps Eqs. (43) with $G_K(x) = K \sin(x)$ the **standard α -Caputo-family of maps**;
- the Riemann-Liouville α -family of maps with $G_K(x) = x - Kx(1-x)$ the **logistic α -RL-family of maps**;
- the Caputo α -family of maps with $G_K(x) = x - Kx(1-x)$ the **logistic α -Caputo-family of maps**.

For $\alpha = 0$ the solution of Eq. (27) and correspondingly, the universal map is identically zero. For $\alpha < 1$ the Riemann-Liouville α -families of maps Eqs. (36) and (37) corresponding to the functions $G_K(x)$ satisfying the condition $G_K(0) = 0$, which is true for the standard and logistic α -RL-families of maps, also produces identically zero.

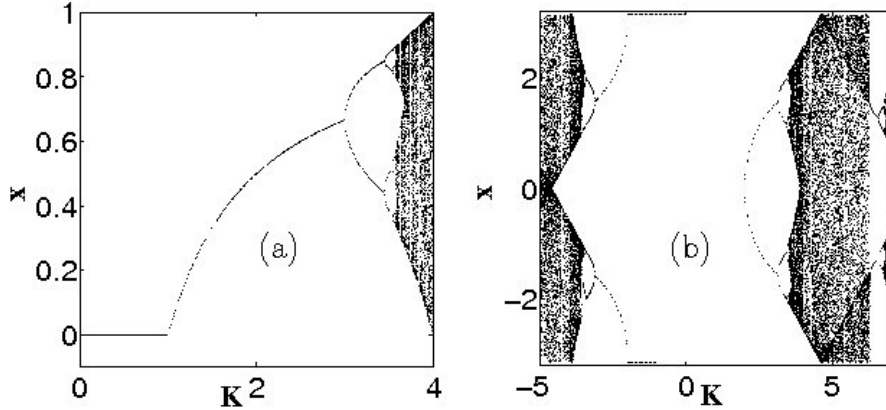


Fig. 2 (a) The bifurcation diagram for the logistic map $x = Kx(1-x)$. (b) The bifurcation diagram for the 1D standard map (circle map) Eq. (47).

3.1 Integer-Dimensional Standard and Logistic Maps

In general, properties of fractional maps converge to the corresponding properties of integer maps when α approaches integer values. To better understand properties of fractional maps we'll start with the consideration of the integer members of the corresponding families of maps.

3.1.1 One-Dimensional Logistic and Standard Maps

The one-dimensional logistic map Eq. (18) is one of the best investigated maps. This map has been used as a playground for investigation of the essential property of nonlinear systems - transition from order to chaos through a sequence of period-doubling bifurcations, which is called cascade of bifurcations, and scaling properties of the corresponding systems (see [2, 15, 24, 42, 84]). In our investigation of fractional maps we'll use the well known stability properties of the logistic map (see [56]), which for $0 < K < 4$ are summarized in the bifurcation diagram in Fig. 2(a). The $x = 0$ fixed point (sink) is stable for $K < 1$, the $(K-1)/K$ fixed point (sink) is stable for $1 < K < 3$, the $T = 2$ sink is stable for $3 \leq K < 1 - \sqrt{6} \approx 3.449$, the $T = 4$ sink is stable when $3.449 < K < 3.544$, and the onset of chaos as a result of the period-doubling cascade of bifurcations occurs at $K \approx 3.56995$.

The one-dimensional standard map ($\alpha = 1$) considered on a circle

$$x_{n+1} = x_n - K \sin(x_n), \quad (\text{mod } 2\pi) \quad (47)$$

is a particular form of the circle map with zero driving phase. It has attracting fixed points $2\pi n$ for $0 < K \leq K_{c1}(1) = 2$ and $\pi + 2\pi n$ when $-2 \leq K < 0$ (for the bifurcation diagram of the 1D standard map see Fig. 2(b)). The antisymmetric $T = 2$

sink

$$x_{n+1} = -x_n \quad (48)$$

is stable for $2 < |K| < \pi$, while $x_{n+1} = x_n + \pi$ two sinks ($T = 2$) are stable when $\pi < |K| < \sqrt{\pi^2 + 2} \approx 3.445$. The stable $T = 4$ sinks appear at $|K| \approx 3.445$ and the sequence of bifurcations $T = 4 \rightarrow T = 8$ at $K \approx 3.513$, $T = 8 \rightarrow T = 16$ at $K \approx 3.526$, and so on leads to the transition to chaos at $K \approx 3.532$. Antisymmetric $T = 2$ trajectories ($K = 2.4$), $T = 4$ trajectories ($K = 3.49$), and two cases of chaotic trajectories ($K = 4.1$ and $K = 5.1$) are presented in Fig. 3. In the 1D standard map with $K > 0$

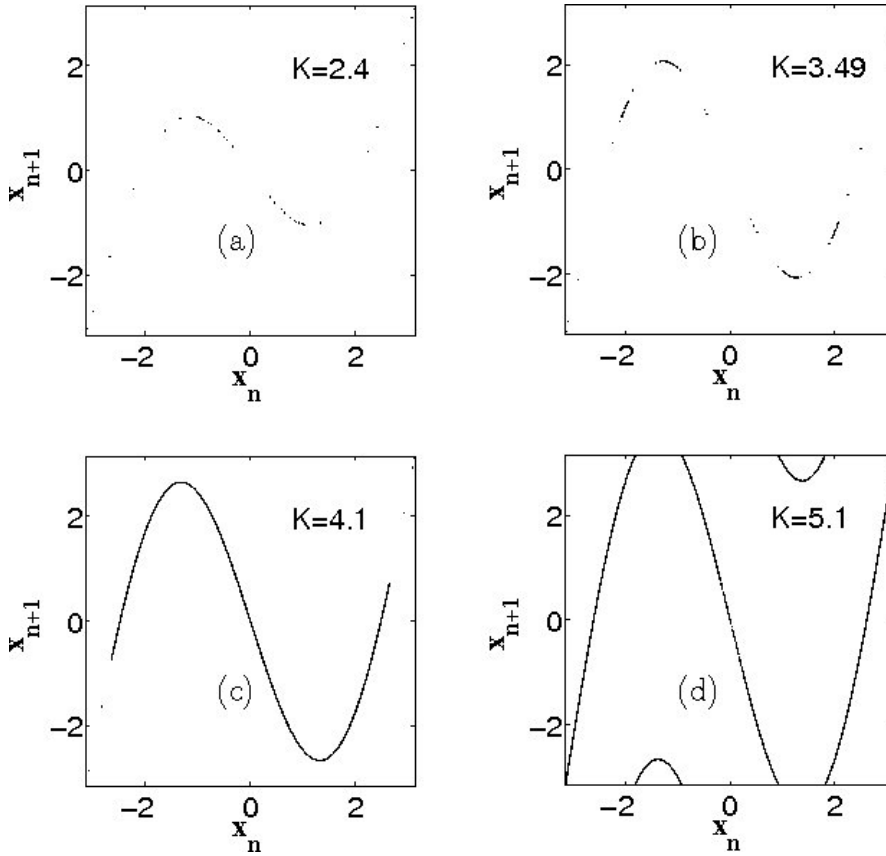


Fig. 3 Attractors in the one-dimensional standard map; x_n vs. x_{n+1} plots (seven trajectories with different initial conditions in each plot): (a). $K = 2.4$; antisymmetric $T = 2$ sink. (b). $K = 3.49$; $T = 4$ trajectories. (c). $K = 4.1$; proper attractor (width of the chaotic area is less than 2π). (d). $K = 5.1$; improper attractor (width of the chaotic area is 2π).

the full phase space $x \in [-\pi, \pi]$ becomes involved in chaotic motion (we'll call this case "improper attractor") when the maximum of the function $f_K(x) = x - K \sin x$ is equal to π which occurs at $K_{max1D} = 4.603339$ when $x_{max1D} = -1.351817$ (see

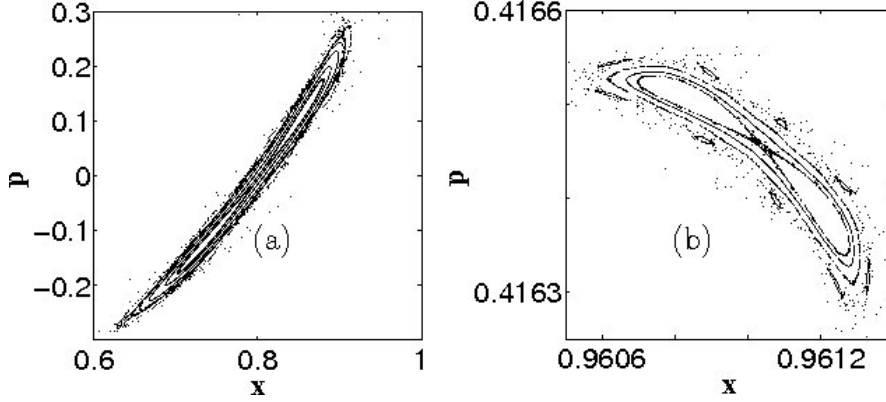


Fig. 4 Bifurcations in the 2D Logistic Map: (a) $T = 1 \rightarrow T = 2$ bifurcation at $K = 5$ ($K = 5.05$ on the figure). (b) $T = 8 \rightarrow T = 16$ bifurcation at $K \approx 5.5319$ ($K = 5.53194$ on the figure).

Figs. 3 (c) and (d)). Narrow bands with $|K|$ above $2\pi|n|$ (see Fig. 2(b) for $K > 2\pi$) are accelerator mode bands with zero acceleration within which in the unbounded space (no mod 2π) x is increasing/decreasing with the rate equal approximately to $2\pi|n|$.

3.1.2 Two-Dimensional Logistic and Standard Maps

The two-dimensional logistic map

$$\begin{aligned} p_{n+1} &= p_n + Kx_n(1 - x_n) - x_n, \\ x_{n+1} &= x_n + p_{n+1} \end{aligned} \quad (49)$$

is a quadratic area preserving map. Its phase space contains stable elliptic islands and chaotic areas (no attractors). Quadratic area preserving maps which have a stable fixed point at the origin were investigated by Hénon [33] (for a recent review on 2D quadratic maps see [94]). To investigate the logistic α -families of maps we need to know the evolution of the periodic points of the 2D logistic map with the increase of the map parameter K . For $K \in (-3, 1)$ the map Eq. (49) has the stable fixed point $(0, 0)$ which turns into the fixed point $((K - 1)/K, 0)$ stable for $K \in (1, 5)$. The $T = 2$ elliptic point

$$\begin{aligned} x &= \frac{K + 3 \pm \sqrt{(K + 3)(K - 5)}}{2K}, \\ p &= \pm \frac{\sqrt{(K + 3)(K - 5)}}{K} \end{aligned} \quad (50)$$

is stable for $-2\sqrt{5} + 1 < K < -3$ and $5 < K < 2\sqrt{5} + 1$. The period doubling

cascade of bifurcations (for $K > 0$) follows the scenario of the elliptic-hyperbolic point transitions with the births of the double periodicity islands inside the original island which has been investigated in [68] and applied to investigate the standard map stochasticity at low values of the map parameter. Further bifurcations in the 2D logistic map, $T = 2 \rightarrow T = 4$ at $K \approx 5.472$, $T = 4 \rightarrow T = 8$ at $K \approx 5.527$, $T = 8 \rightarrow T = 16$ at $K \approx 5.5319$, $T = 16 \rightarrow T = 32$ at $K \approx 5.53253$, etc., and the corresponding decrease in the areas of the islands of stability (see Fig. 4) lead to chaos.

The two-dimensional standard map on a torus Eq. (17) (Chirikov standard map) is one of the best investigated 2D maps. It demonstrates a universal generic behavior of the area-preserving maps whose phase space is divided into elliptic islands of stability and areas of chaotic motion (see, e.g., [11, 45]). Elliptic islands of the standard map in the case of the standard α -families of maps with $1 < \alpha < 2$ evolve into periodic sinks (see Sec. 3.3). Properties of phase space and appearance of different types of attractors in the fractional case, as in the case of the fractional logistic map, are connected to the evolution (with the increase in parameter K) of the 2D standard map's islands originating from the stable (for $K < 4$) fixed point (0,0). At $K = 4$ the fixed point becomes unstable (elliptic-hyperbolic point transition [68]) and two elliptic islands around the stable for $4 < K < 2\pi$ period 2 antisymmetric point

$$p_{n+1} = -p_n, \quad x_{n+1} = -x_n \quad (51)$$

appear. At $K = 2\pi$ this point transforms into two $T = 2$ points

$$p_{n+1} = -p_n, \quad x_{n+1} = x_n - \pi, \quad (52)$$

which are stable when $2\pi < K < 6.59$. These points transform into $T = 4$ stable elliptic points at $K \approx 6.59$ and the period doubling cascade of bifurcations leads to the disappearance of islands of stability in the chaotic sea at $K \approx 6.6344$ [11, 45]. The 2D standard map has a set of bands for K above $2\pi n$ of the accelerator mode sticky islands in which the momentum p increases proportionally to the number of iterations k and the coordinate x increases as k^2 . The role of accelerator mode islands (for K above 2π) in the anomalous diffusion and the corresponding fractional kinetics is well investigated (see, for example, [90, 93]).

3.1.3 Three-Dimensional Logistic and Standard Maps

Eq. (46) with $G_K(x) = x - Kx(1-x)$ (see Eq. (26) produces the 3D logistic map

$$\begin{aligned} x_{n+1} &= x_n + y_{n+1} - \frac{1}{2}z_{n+1}, \\ y_{n+1} &= y_n + z_{n+1}, \\ z_{n+1} &= Kx_n(1-x_n) - x_n + z_n. \end{aligned} \quad (53)$$

Three-dimensional quadratic volume preserving maps were investigated in [58, 46]. Everything stated in Sec. 3 for the 3D universal map is still valid for the 3D logistic map.

The three-dimensional standard map with $G_K(x) = K \sin(x)$

$$\begin{aligned} x_{n+1} &= x_n + y_{n+1} - \frac{1}{2}z_{n+1}, \pmod{2\pi}, \\ y_{n+1} &= y_n + z_{n+1}, \pmod{2\pi}, \\ z_{n+1} &= -K \sin(x_n) + z_n, \pmod{4\pi} \end{aligned} \quad (54)$$

has unstable fixed points $(2\pi n, 2\pi m, 4\pi k)$ and $(2\pi n + \pi, 2\pi m, 4\pi k)$, $n \in \mathbb{Z}$, $m \in \mathbb{Z}$, $k \in \mathbb{Z}$. Ballistic points $K \sin(x) = -4\pi n$, $y = 2\pi m$, $z = 4\pi k$, which appear for $|K| \geq 4\pi$, are also unstable.

Stability of $T = 2$ ballistic points is defined by the eigenvalues of the matrix

$$\begin{pmatrix} 1 - 0.5K \cos x_1 & 1 & 0.5 \\ -K \cos x_1 & 1 & 1 \\ -K \cos x_1 & 0 & 1 \end{pmatrix} \times \begin{pmatrix} 1 - 0.5K \cos x_2 & 1 & 0.5 \\ -K \cos x_2 & 1 & 1 \\ -K \cos x_2 & 0 & 1 \end{pmatrix}.$$

For the period two on the torus ballistic points

$$\begin{aligned} z_1, y_1 &= \frac{z_1}{2} - \pi(2n+1), \quad K \sin x_1 = 2z_1, \\ z_2 = -z_1, y_2 &= -\frac{z_1}{2} - \pi(2n+1), \quad x_2 = x_1 - \pi(2n-1), \end{aligned} \quad (55)$$

where $n \in \mathbb{Z}$, the eigenvalues are

$$\left\{ 1, \frac{1}{8}(8 - K^2 \cos^2 x_1 \pm K \cos x_1 \sqrt{K^2 \cos^2 x_1 - 16}) \right\} \quad (56)$$

Ballistic $T = 2$ points are stable along a line defined by Eqs. (55) for all values of z satisfying the condition

$$K^2 - 16 < 4z^2 < K^2. \quad (57)$$

An example of the phase space for $K = 3$ in three dimensions and its projection on the x - y plane is given in Fig. 5. For this value of K ballistic $T = 2$ points are stable when $-1.5 < z < 1.5$ and the space around the line of stability presents a series of islands (invariant curves), islands around islands, and separatrix layers. When $K \rightarrow 0$, the volume of the regular motion shrinks. When K is small, the line of the stable $T = 2$ ballistic points exists for $-K/2 < z < K/2$. A different form of the 3D volume preserving standard map was introduced and investigated in detail in [18].

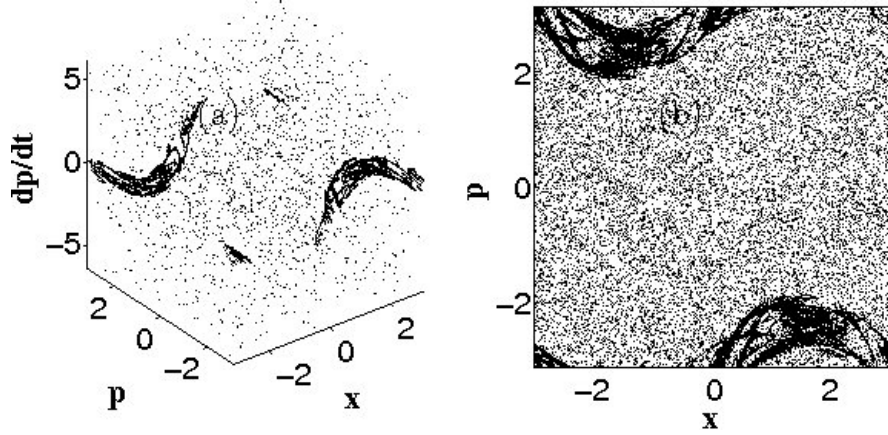


Fig. 5 Phase space of the 3D standard map (54) with $K = 3$: (a). Three dimensional phase space. (b). A projection of the 3D phase space on the x - y plane.

3.2 α -Families of Maps ($0 < \alpha < 1$)

As we mentioned at the end of Sec. 3, members of the logistic and standard α -families of maps corresponding to $\alpha = 0$ and RL-families' members with $0 < \alpha < 1$ are identically zeros. The only fractional logistic and standard maps with $0 < \alpha < 1$ which are not identically zeros are α -Caputo-families of maps. The α -Caputo-universal map ($0 < \alpha < 1$)

$$x_{n+1} = x_0 - \frac{1}{\Gamma(\alpha)} \sum_{k=0}^n G_K(x_k) (n-k+1)^{\alpha-1} \quad (58)$$

in the limit $\alpha \rightarrow 1$ is identical to the one-dimensional universal map Eq. (25) and in this limit properties of fractional maps are similar to properties of the corresponding 1D maps. Eq. (58) with $G_K(x) = x - Kx(1-x)$ is the logistic α -Caputo-family of maps for $0 < \alpha < 1$

$$x_n = x_0 + \frac{1}{\Gamma(\alpha)} \sum_{k=0}^{n-1} \frac{Kx_k(1-x_k) - x_k}{(n-k)^{1-\alpha}} \quad (59)$$

and with $G_K(x) = K \sin(x)$ is the standard α -Caputo-family of maps for $0 < \alpha < 1$

$$x_n = x_0 - \frac{K}{\Gamma(\alpha)} \sum_{k=0}^{n-1} \frac{\sin x_k}{(n-k)^{1-\alpha}}, \quad (\text{mod } 2\pi) \quad (60)$$

These maps are one-dimensional maps with power-law decreasing memory [20]. The bifurcation diagrams for these maps are similar to the corresponding diagrams for the $\alpha = 1$ case Fig. 2. A decrease in α and the corresponding decrease in weights

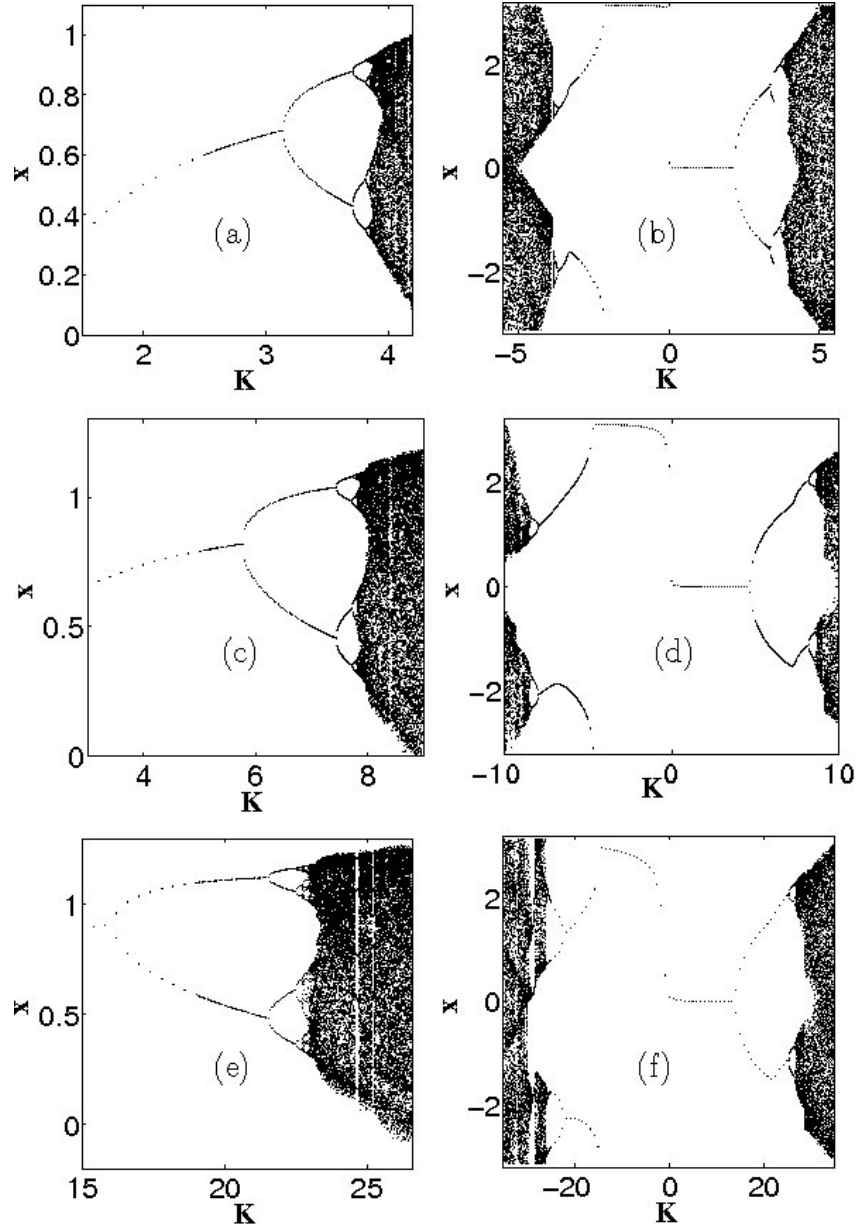


Fig. 6 Bifurcation diagrams for the logistic and standard α -Caputo-families of maps with $0 < \alpha < 1$. In (a)-(f) the bifurcation diagrams obtained after performing 10^4 iterations on a single trajectory with $x_0 = 0.1$ for various values of K . (a), (c), and (e) - the logistic α -Caputo-family. (b), (d), and (f) - the standard α -Caputo-family. In (a) and (b) $\alpha = 0.8$. In (c) and (d) $\alpha = 0.3$. In (e) and (f) $\alpha = 0.1$.

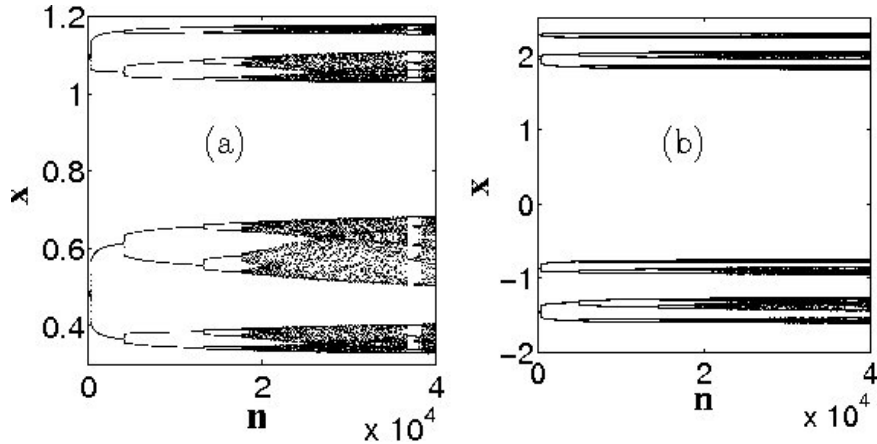


Fig. 7 Cascade of bifurcations type trajectories in the logistic and standard α -Caputo-families of maps with $\alpha = 0.1$. (a) The fractional logistic map with $\alpha = 0.1$ and $K = 22.65$. (b) The fractional standard map with $\alpha = 0.1$ and $K = 26.65$.

of the earlier states (decrease in memory effects) leads to the stretchiness of the corresponding bifurcation diagrams along the parameter K -axis and this stretchiness increases as α gets smaller Fig. 6.

Within a band of values of K , above the value which corresponds to the appearance of $T = 4$ trajectories, map trajectories are attracting cascade of bifurcations type trajectories (CBTT) (see Fig. 7). On CBTT an increase in the number of map iterations leads to the change in the map's stability properties. A trajectory which converges to a $T > 4$ periodic point or becomes a chaotic trajectory (depending on the value of K) evolves according to a certain scenario: it first converges to a $T = 4$ point; then it bifurcates, always at the same place for the given values of the parameter K and the order α , and converges to a $T = 8$ trajectory; then to a $T = 16$ trajectory; and so on. Power-law decaying memory with power $\beta \approx 0.9$ corresponding to small values of $\alpha \approx 0.1$ (see Sec. 1.1) appears in biological applications. Attracting CBTT in, for example, adaptive biological systems may represent not simply a change of a state of a biological system according to a change in a parameter, but rather a change in the evolution of the system according to the change in the parameter. Examples of CBTT in the logistic and standard α -Caputo-families of maps with $\alpha = 0.1$ are presented in Fig. 7.

It also should be noted that bifurcation diagrams of the fractional maps depend on the number of iterations used in their calculations. This is a consequence of the existence of CBTT. Trajectories which after 100 iterations converged to a fixed point in Fig. 8(b) after 10000 iterations became $T = 2$ trajectories in Fig. 8(a). With an increase in the number of iterations the whole bifurcation diagram shifts to the left.

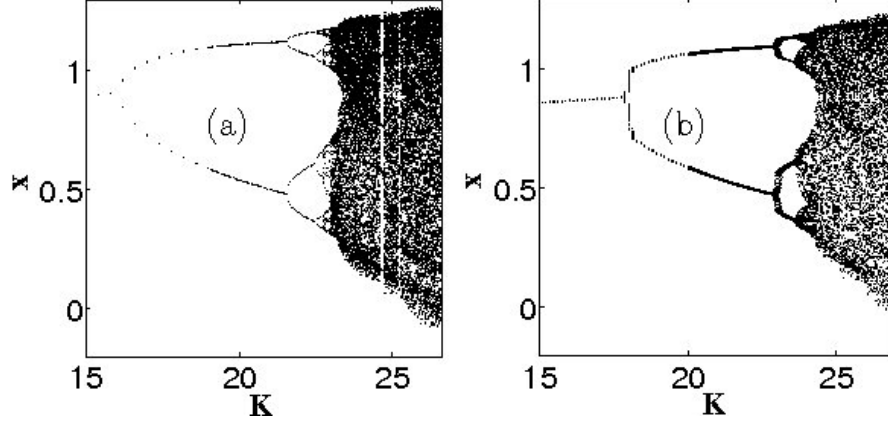


Fig. 8 Dependence of bifurcation diagrams of the fractional maps on the number of iterations on a single trajectory used in their calculation. Bifurcation diagrams for the fractional logistic map with $\alpha = 0.1$. (a) 10000 iterations on each trajectory. (b) 100 iterations on each trajectory.

3.3 α -Families of Maps ($1 < \alpha < 2$)

For $1 < \alpha < 2$ the logistic and standard α -families of maps assume the following forms:

- The RL-standard map on a cylinder

$$p_{n+1} = p_n - K \sin x_n, \quad (61)$$

$$x_{n+1} = \frac{1}{\Gamma(\alpha)} \sum_{i=0}^n p_{i+1} V_\alpha^1(n-i+1), \quad (\text{mod } 2\pi), \quad (62)$$

where

$$V_\alpha^k(m) = m^{\alpha-k} - (m-1)^{\alpha-k}. \quad (63)$$

This map requires the initial condition $x_0 = 0$ and can't be considered on a torus.

- The Caputo-standard map on a torus

$$p_{n+1} = p_n - \frac{K}{\Gamma(\alpha-1)} \left[\sum_{i=0}^{n-1} V_\alpha^2(n-i+1) \sin x_i + \sin x_n \right], \quad (\text{mod } 2\pi), \quad (64)$$

$$x_{n+1} = x_n + p_0 - \frac{K}{\Gamma(\alpha)} \sum_{i=0}^n V_\alpha^1(n-i+1) \sin x_i, \quad (\text{mod } 2\pi). \quad (65)$$

- The RL-logistic map

$$p_{n+1} = p_n - Kx_n(1-x_n) - x_n, \quad (66)$$

$$x_{n+1} = \frac{1}{\Gamma(\alpha)} \sum_{i=0}^n p_{i+1} V_\alpha^1(n-i+1), \quad (67)$$

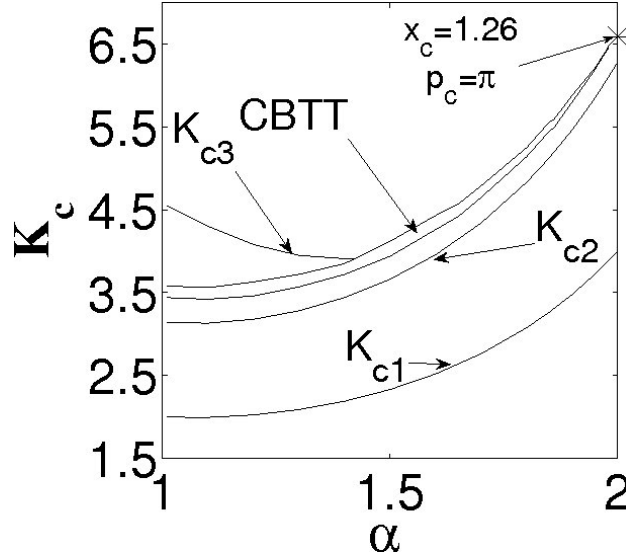


Fig. 9 Bifurcations in the standard α -families of maps with $1 < \alpha < 2$. Below $K = K_{c1}$ curve the fixed point $(0,0)$ is stable. It becomes unstable at $K = K_{c1}$ and gives birth to the antisymmetric $T = 2$ sink which is stable for $K_{c1} < K < K_{c2}$. A pair of the $T = 2$ sinks with $x_{n+1} = x_n - \pi$, $p_{n+1} = -p_n$ is stable in the band above $K = K_{c2}$ curve. Cascade of bifurcations type trajectories (CBTT) appear and exist in the narrow band which ends at the cusp at the top right corner of the figure. (x_c, p_c) is the point at which the standard map's $(\alpha = 2)$ $T = 2$ elliptic points with $x_{n+1} = x_n - \pi$, $p_{n+1} = -p_n$ become unstable and bifurcate. In the area below K_{c3} (above the CBTT band) the chaotic attractor is restricted to a band whose width is less than 2π . On the upper curves and above them the full phase space is chaotic.

which requires the initial condition $x_0 = 0$.

- The Caputo-logistic map

$$x_{n+1} = x_0 + p(n+1)^k - \frac{1}{\Gamma(\alpha)} \sum_{k=0}^n [x_k - Kx_k(1-x_k)](n-k+1)^{\alpha-1}, \quad (68)$$

$$p_{n+1} = p_0 - \frac{1}{\Gamma(\alpha-1)} \sum_{k=0}^n [x_k - Kx_k(1-x_k)](n-k+1)^{\alpha-2}. \quad (69)$$

Here and in Eqs. (64) and (65) we assumed $x \equiv x^0$ and $p \equiv x^1$ in the Caputo universal map Eq. (43).

The fractional standard maps Eqs. (61), (62), (64), and (65) are well investigated (see [19, 20, 21, 22]) and the logistic maps are the subject of ongoing research.

Evolution of trajectories in fractional maps depends on two parameters: the map parameter K and the fractional order α . Fig. 9 reflects this dependence in the case of the standard α -families of maps with $1 < \alpha < 2$.

3.3.1 $T = 2$ Antisymmetric Sink

It is obvious that the fractional standard and logistic maps have the fixed points at the origin $(0, 0)$. But we'll start the fractional maps' phase space analysis with the consideration of the $T = 2$ antisymmetric sinks. We'll present most of the analysis for the fractional RL-standard map (Fig. 9). Results of numerical simulations suggest that the fractional Caputo-standard map has similar properties and the results for the logistic map are submitted for publication.

The 1D standard map has the $T = 2$ antisymmetric sink Eq. (48) and the 2D standard map has the $T = 2$ antisymmetric elliptic point Eq. (51). Numerical experiments (Fig. 10) show that the antisymmetric $T = 2$ sinks persist in the fractional standard maps with $1 < \alpha < 2$. In the RL-standard map these sinks in the RL-standard map attract most of the trajectories with small p_0 . Assuming the existence of an antisymmetric $T = 2$ sink

$$p_n = p_l(-1)^n, \quad x_n = x_l(-1)^n, \quad (70)$$

it is possible to calculate the coordinates of its attracting points (x_l, p_l) and $(-x_l, -p_l)$. In the limit $n \rightarrow \infty$ Eqs. (61) and (62) can be written as

$$p_l = \frac{K}{2} \sin(x_l), \quad (71)$$

$$x_l = \lim_{n \rightarrow \infty} x_{2n} = \frac{p_l}{\Gamma(\alpha)} \lim_{n \rightarrow \infty} \sum_{k=0}^{2n-1} (-1)^{k+1} V_\alpha^1(2n-i) = \frac{p_l}{\Gamma(\alpha)} V_{\alpha l}(k), \quad (72)$$

where

$$V_{\alpha l} = \sum_{k=1}^{\infty} (-1)^{k+1} V_\alpha^1(k). \quad (73)$$

Finally, the equation for the x_l takes the form

$$x_l = \frac{K}{2\Gamma(\alpha)} V_{\alpha l} \sin(x_l). \quad (74)$$

The numerical solution of Eqs. (74) and (71) for $K = 4.5$ when $1 < \alpha < 2$ is presented in Figs. 10 (b)-(d). Figs. 10 (e) and (f) show how well this solution agrees with the results of numerical simulations of individual trajectories. After 1000 iterations presented in Figs. 10 (e) and (f) the values of deviations $|p_n - p_l|$ and $|x_n - x_l|$ are less than 10^{-7} .

The condition of the existence of a solution for Eq. (74)

$$K > K_{c1}(\alpha) = \frac{2\Gamma(\alpha)}{V_{\alpha l}} \quad (75)$$

is the condition of the existence of the antisymmetric $T = 2$ sink. This sink exists above the curve $K = K_{c1}$ on Fig. 9. For $\alpha = 2$ Eq. (75) produces the standard map condition $K > 4$ (see Sec 3.1.2) and for $\alpha = 1$ it gives $K > 2$ (see Sec 3.1.1).

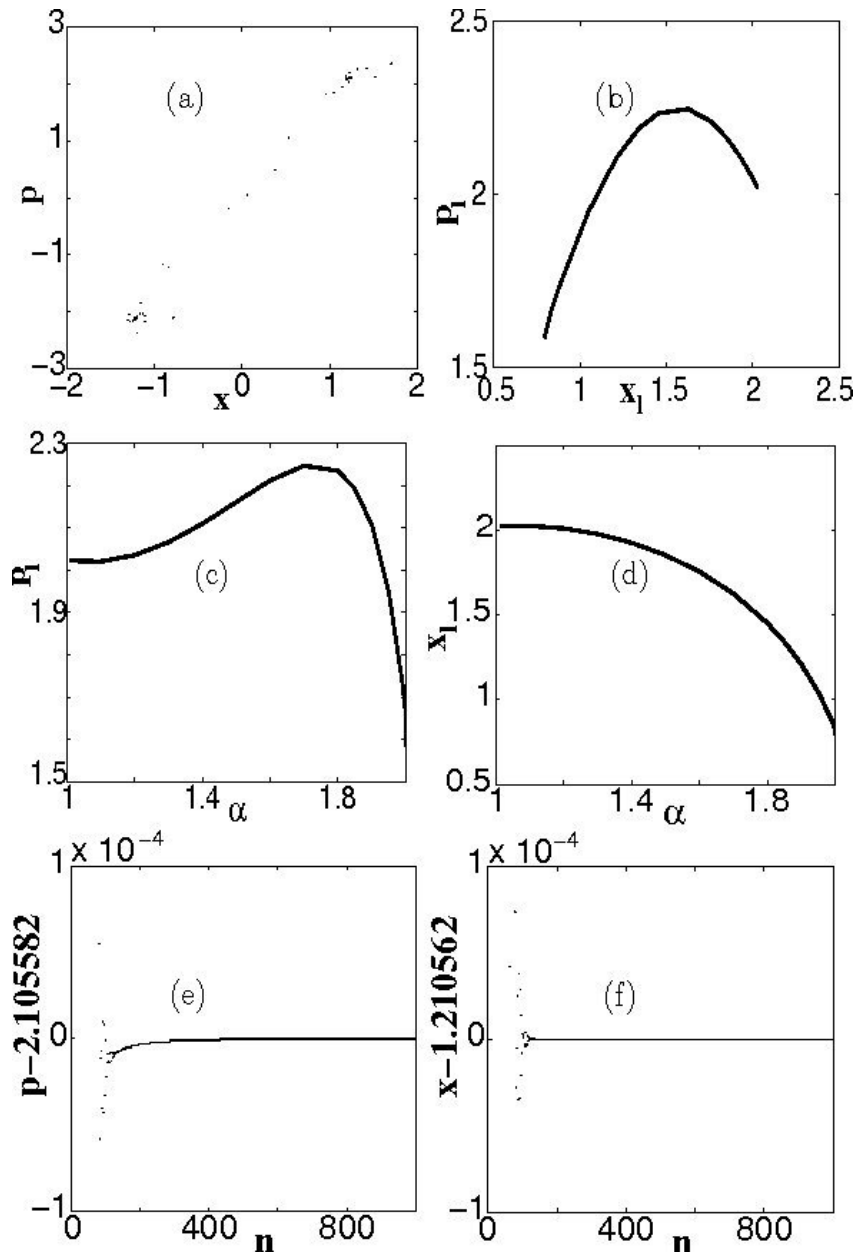


Fig. 10 The RL-standard map's period 2 sink: (a). An example of the $T = 2$ attractor for $K = 4.5$, $\alpha = 1.9$. One trajectory with $x_0 = 0$, $p_0 = 0.513$. (b). p_l of x_l for the case of $K = 4.5$. (c). p_l of α for the case of $K = 4.5$. (d). x_l of α for the case of $K = 4.5$. (e). $p_n - p_l$ for the trajectory in (a). After 1000 iterations $|p_n - p_l| < 10^{-7}$. (f). $x_n - x_l$ for the trajectory in (a). After 1000 iterations $|x_n - x_l| < 10^{-7}$.

3.3.2 Fixed Points

Numerical simulations show that as in the 1D and 2D cases, in the case of fractional maps with $1 < \alpha < 2$ the condition of the appearance of $T = 2$ trajectories coincides with the condition of the disappearance of the stable fixed point. This result for the fractional standard map was demonstrated in [22] and for the fractional logistic map was submitted for publication. Below we present two ways in which stability of the RL-standard map's $(0, 0)$ fixed point can be investigated.

In the vicinity of the fixed point $(0, 0)$ the equation for the deviation of a trajectory from the fixed point can be written as

$$\delta p_{n+1} = \delta p_n - K \delta x_n, \quad (76)$$

$$\delta x_{n+1} = \frac{1}{\Gamma(\alpha)} \sum_{i=0}^n \delta p_{i+1} V_\alpha(n-i+1). \quad (77)$$

Based on the results of Sec. 3.3.1 let's look for a solution in the form

$$\delta p_n = p_0 \sum_{i=0}^{n-1} p_{n,i} \left(\frac{2}{V_{\alpha l}}\right)^i \left(\frac{K}{K_{c1}(\alpha)}\right)^i, \quad (n > 0), \quad (78)$$

$$\delta x_n = \frac{p_0}{\Gamma(\alpha)} \sum_{i=0}^{n-1} x_{n,i} \left(\frac{2}{V_{\alpha l}}\right)^i \left(\frac{K}{K_{c1}(\alpha)}\right)^i, \quad (n > 0), \quad (79)$$

where $p_{n,i}$ and $x_{n,i}$ satisfy the following iterative equations

$$x_{n+1,i} = - \sum_{m=i}^n (n-m+1)^{\alpha-1} x_{m,i-1}, \quad (0 < i \leq n), \quad (80)$$

$$p_{n+1,i} = - \sum_{m=i}^n x_{m,i-1}, \quad (0 < i < n), \quad (81)$$

for which the initial and boundary conditions are

$$p_{n+1,n} = x_{n+1,n} = (-1)^n, \quad p_{n+1,0} = 1, \quad x_{n+1,0} = (n+1)^{\alpha-1}. \quad (82)$$

To verify the convergence of the alternating series Eqs. (78) and (79) we apply the Dirichlet's test by considering the totals

$$S_n = \sum_{i=0}^{n-1} x_{n,i} \left(\frac{2}{V_{\alpha l}}\right)^i, \quad I_n = \sum_{i=0}^{n-1} p_{n,i} \left(\frac{2}{V_{\alpha l}}\right)^i. \quad (83)$$

They obey the following iterative rules

$$S_n = n^{\alpha-1} - \frac{2}{V_{\alpha l}} \sum_{i=1}^{n-1} (n-i)^{\alpha-1} S_i, \quad I_n = 1 - \frac{2}{V_{\alpha l}} \sum_{i=1}^{n-1} S_i, \quad (84)$$

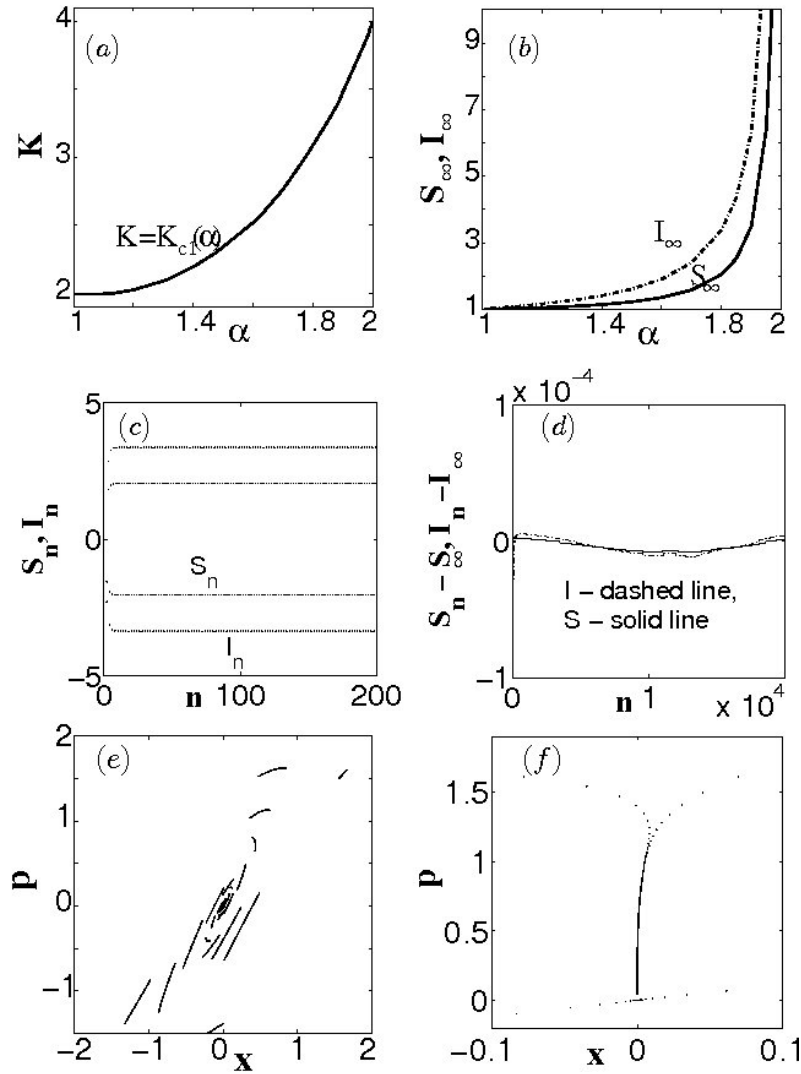


Fig. 11 Stability of the fixed point $(0,0)$ in the RL-standard map with $1 < \alpha < 2$: (a). The fixed point is stable below the curve $K = K_c(\alpha)$. (b). Values of S_∞ and I_∞ obtained after 20000 iterations of Eq. 84. The values of S_∞ and I_∞ increase rapidly when $\alpha \rightarrow 2$; for example, $S_\infty \approx 276$ and $I_\infty \approx 552$ after 20000 iterations when $\alpha = 1.999$. (c). An example of the typical evolution of S_∞ and I_∞ over the first 200 iterations for $1 < \alpha < 2$. This particular figure corresponds to $\alpha = 1.8$. (d). Deviation of the values S_n and I_n from the values $S_\infty \approx 2.04337$ and $I_\infty \approx 3.37416$ for $\alpha = 1.8$ during the first 20000 iterations (this type of behavior remains for $1 < \alpha < 2$). (e). Evolution of trajectories with $p_0 = 1.5 + 0.0005i$, $0 \leq i < 200$ for the case $K = 3$, $\alpha = 1.9$. The line segments correspond to the n th iteration on the set of trajectories with close initial conditions. The evolution of the trajectories with smaller p_0 is similar. (f). 10^5 iterations on both of two trajectories for $K = 2$, $\alpha = 1.4$. The one at the bottom with $p_0 = 0.3$ is a fast converging trajectory. The upper trajectory with $p_0 = 5.3$ is an example of an attracting slow converging trajectory in which $p_{100000} \approx 0.042$.

where $S_1 = 1$. Numerical simulations demonstrate that values of S_n and I_n converge to the values $(-1)^{n+1}S_\infty$ and $(-1)^{n+1}I_\infty$ presented in Fig. 11(b). Figs. 11(c) and (d) show an example of the typical evolution of S_n and I_n over the first 20000 iterations. There is still no strict mathematical proof of the convergence. From the boundedness of S_n and I_n the convergence of δp_n and δx_n requires the following condition

$$\frac{K}{K_{c1}(\alpha)} < 1, \quad (85)$$

which, as we expected, is exactly opposite to the condition of the existence of the antisymmetric $T = 2$ sink Eq. (75). Hundreds of runs of computer simulations confirmed that the transition from the stable fixed point $(0,0)$ to the stable antisymmetric $T = 2$ sink in both the RL-standard map and the Caputo-standard map occurs on the curve $K = K_{c1}$ depicted in Fig. 11(a).

The second way to investigate stability of the $(0,0)$ fixed point is by using generating functions [25], which in the case of convolutions allows transformations of sums of products into products of sums. After the introduction

$$\tilde{W}_\alpha(t) = \frac{K}{\Gamma(\alpha)} \sum_{i=0}^{\infty} [(i+1)^{\alpha-1} - i^{\alpha-1}] t^i, \quad \tilde{X}(t) = \sum_{i=0}^{\infty} \delta x_i t^i, \quad \tilde{P}(t) = \sum_{i=0}^{\infty} \delta p_i t^i \quad (86)$$

system Eqs. (76) and (77) can be written as

$$\tilde{X}(t) = \frac{p_0 \tilde{W}_\alpha(t)}{K} \frac{t}{1 - t(1 - \tilde{W}_\alpha(t))}, \quad (87)$$

$$\tilde{P}(t) = p_0 \frac{1 + \tilde{W}_\alpha(t)}{1 - t(1 - \tilde{W}_\alpha(t))}. \quad (88)$$

We see that the original problem can be solved by investigating the asymptotic behavior at $t = 0$ of the derivatives of the analytic functions $\tilde{X}(t)$ and $\tilde{P}(t)$. This is still a complex unresolved problem.

When $K < K_{c1}$ and the fixed point is stable, in phase space it is surrounded by a finite basin of attraction, whose width w depends on the values of K and α . For example, for $K = 3$ and $\alpha = 1.9$ the width of the basin of attraction is $1.6 < w < 1.7$. Numeric simulations of thousands of trajectories with $p_0 < 1.6$ performed by the authors of [22], of which only 200 (with $1.5 < p_0 < 1.6$) are presented in Fig. 11(e), show only converging trajectories, whereas among 50 trajectories with $1.6 < p_0 < 1.7$ in Fig. 12(a) there are trajectories converging to the fixed point as well as some trajectories converging to attracting slow diverging trajectories, whose properties will be discussed in the following section (Sec. 3.3.3). Fig. 11(e) shows fast converging trajectories. In the case $K = 2$ and $\alpha = 1.4$ in addition to the fast converging trajectories and attracting slow diverging trajectories there exist attracting slow converging trajectories (Fig. 11(f)).

3.3.3 Attractors Below Cascade of Bifurcations Band

In the following most of the statements are conjectures made on the basis of the results of numerical simulations performed for some values of parameters K and α which then were verified for additional parameter values.

The structure of the fractional standard map's phase space preserves some features which exist in the $\alpha = 2$ case. For example, for $K < K_{c1}$ stable higher period points, which exist in the standard map, still exist in the fractional standard maps Fig. 12, but they exist in the asymptotic sense and they transform from elliptic points into sinks and (in the case of the RL-standard map) into attracting slow ($p_n \sim n^{2-\alpha}$) diverging trajectories. In the area preserving standard map stable fixed and periodic points are surrounded by islands of regular motion which in the case of fractional maps turn into basins of attraction associated with sinks or slowly diverging attracting trajectories. In the standard map islands are surrounded by chaotic areas. For $K < K_{c1}$ and $1 < \alpha < 2$ in the fractional standard maps there are no chaotic or regular trajectories. Chaos exists in the following sense: two initially close trajectories that start in an area between basins of attractions at first diverge, but then converge to the same or different attractors.

There are differences not only between properties of the regular and fractional standard maps but also between phase space structures of the RL- and Caputo-standard maps. There is more than one way to approach an attracting periodic or fixed point of the RL-standard map. In Fig. 13 the examples of three trajectories, two for the RL-standard map and one for the Caputo-standard map, are used to demonstrate the differences in the rates of convergence. In the RL-standard map trajectories starting from attractors' basins of attractions demonstrate fast convergence with

$$\delta x_n \sim n^{-1-\alpha}, \quad \delta p_n \sim n^{-\alpha} \quad (89)$$

and trajectories with the initial conditions from chaotic areas demonstrate slow convergence:

$$\delta x_n \sim n^{-\alpha}, \quad \delta p_n \sim n^{1-\alpha}. \quad (90)$$

There is only one type of convergence in the Caputo-standard map:

$$\delta x_n \sim n^{1-\alpha}, \quad \delta p_n \sim n^{1-\alpha}. \quad (91)$$

The same rates of convergence were observed also for antisymmetric (see Sec. 3.3.1 and Fig. 15) and $x_{n+1} = x_n - \pi$, $p_{n+1} = -p_n$ period two ($T = 2$) points (Fig. 16).

From Figs. 15 (a) and (b) one can see that phase portraits on cylinders of the fractional standard maps with $K = 3$ and $\alpha = 1.9$ contain, in addition to the $(0, 0)$ fixed point, attracting slow diverging trajectories (RL-case), or fixed points (Caputo-case) approximately equally spaced along the p -axis. This result agrees with the fact that the standard map with $K = 3$ has only one central island. More complex structures of the fractional standard maps' phase spaces, for $K = 2$ with $T = 4$ sinks (Figs. 15 (c) and (d)) and for $K = 0.6$ with $T = 2$ and $T = 3$ sinks (Figs. 15 (e) and (f)), can be explained by the presence of the islands with the same

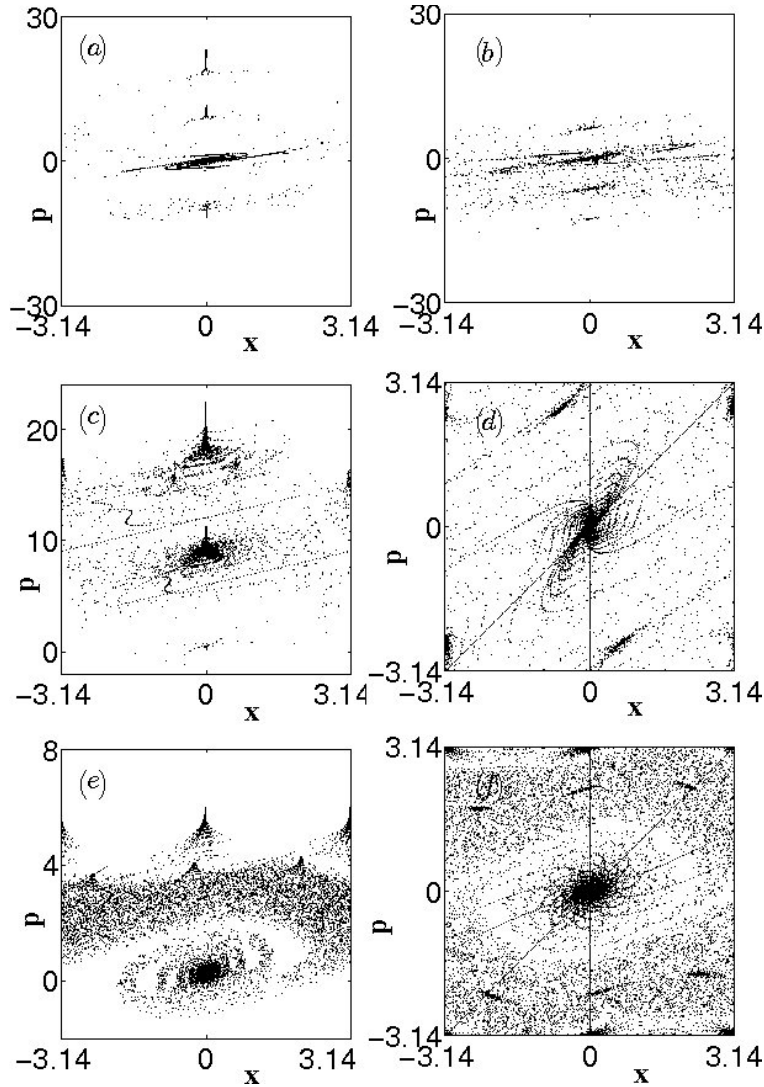


Fig. 12 The RL- and Caputo-standard maps' phase spaces for $K < Kc1$: (a). The RL-standard map with the same values of parameters as in Fig. 11(e) but $p_0 = 1.6 + 0.002i$, $0 \leq i < 50$. (b). The Caputo-standard map with the same values of parameters as in Fig. 11(e) but $p_0 = 1.7 + 0.002i$, $0 \leq i < 50$. (c). 400 iterations on the RL-standard map trajectories with $p_0 = 4 + 0.08i$, $0 \leq i < 125$ for the case $K = 2$, $\alpha = 1.9$. Trajectories converge to the fixed point and two types of attracting slow diverging trajectories: with $x_{lim} = 0$ ($T = 1$) and $T = 4$. (d). 100 iterations on the Caputo-standard map trajectories with $p_0 = -3.14 + 0.0314i$, $0 \leq i < 200$ for the same case as in (c) ($K = 2$, $\alpha = 1.9$) but considered on a torus. In this case all trajectories converge to the fixed point or $T = 4$ sink. (e). 400 iterations on trajectories with $p_0 = 2 + 0.04i$, $0 \leq i < 50$ for the RL-standard map case $K = 0.6$, $\alpha = 1.9$. Trajectories converge to the fixed point and two attracting slow diverging trajectories ($T = 2$ and $T = 3$). (f). 100 iterations on the Caputo-standard map trajectories with $p_0 = -3.14 + 0.0314i$, $0 \leq i < 200$ for the same case as in (e) ($K = 0.6$, $\alpha = 1.9$) considered on a torus. In this case all trajectories converge to the fixed point, period two and period three sinks.

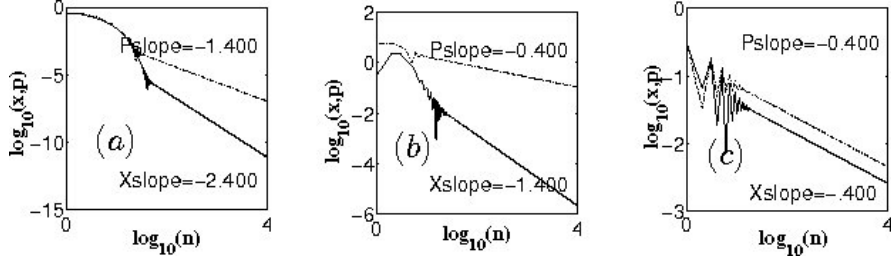


Fig. 13 Different types of convergence of trajectories to the fixed point in the RL-standard map ((a) and (b)) and the Caputo-standard map (c): (a). Time dependence of the coordinate and momentum for the fast converging trajectory with $K = 2$, $\alpha = 1.4$ and the initial conditions $x_0 = 0$ and $p_0 = 0.3$ from Fig. 11(f). (b). The same as in (a) but for the attracting slow converging trajectory with the initial conditions $x_0 = 0$ and $p_0 = 5.3$. (c). x and p time dependence for the Caputo-standard map with $K = 2$, $\alpha = 1.4$, and the initial conditions $x_0 = 0$ and $p_0 = 0.3$.

periodicity in the standard map with the same K . Numerical evaluations (see Fig. 14) lead to the suggestion that attracting slow diverging trajectories which converge to trajectories along the p -axis ($x \rightarrow x_{lim} = 0$) in the area of parameters of their stability for large n demonstrate the following asymptotic behavior

$$p_n = Cn^{2-\alpha}. \quad (92)$$

The constant C can be evaluated for $1.8 < \alpha < 2$. Consider a trajectory on a cylinder with $x_{lim} = 0$, $T = 1$, and constant step in x in the unbounded space $2\pi M$, where M is an integer. Then from Eq. (62) follows

$$x_{n+1} - x_n = \frac{1}{\Gamma(\alpha)} \sum_{k=1}^n (p_{k+1} - p_k) V_\alpha^1(n-k+1) + \frac{p_1}{\Gamma(\alpha)} V_\alpha^1(n+1). \quad (93)$$

For large n the last term is small ($\sim n^{\alpha-2}$) and the following holds

$$\sum_{k=1}^n (p_{k+1} - p_k) V_\alpha^1(n-k+1) = 2\pi M \Gamma(\alpha). \quad (94)$$

It can be shown, assuming $p_n \sim n^{2-\alpha}$, that for values of $\alpha > 1.8$ the terms in the last sum with large k are small and in the series representation of $V_\alpha^1(n-k+1)$ only terms of the highest order in k/n can be kept. In this case, Eq. (94) leads to the approximations

$$p_n \approx p_0 + \frac{2\pi M \Gamma(\alpha) n^{2-\alpha}}{\alpha-1}, \quad x_n \approx -\frac{2\pi M (2-\alpha) \Gamma(\alpha)}{K(\alpha-1) n^{\alpha-1}}. \quad (95)$$

In the case $K = 2$, $\alpha = 1.9$ Figs. 14 (b)-(d) show for two trajectories with $M = 1$ (initial momenta $p_0 = 6$ and $p_0 = 7$) approaching an attracting slow diverging trajectory

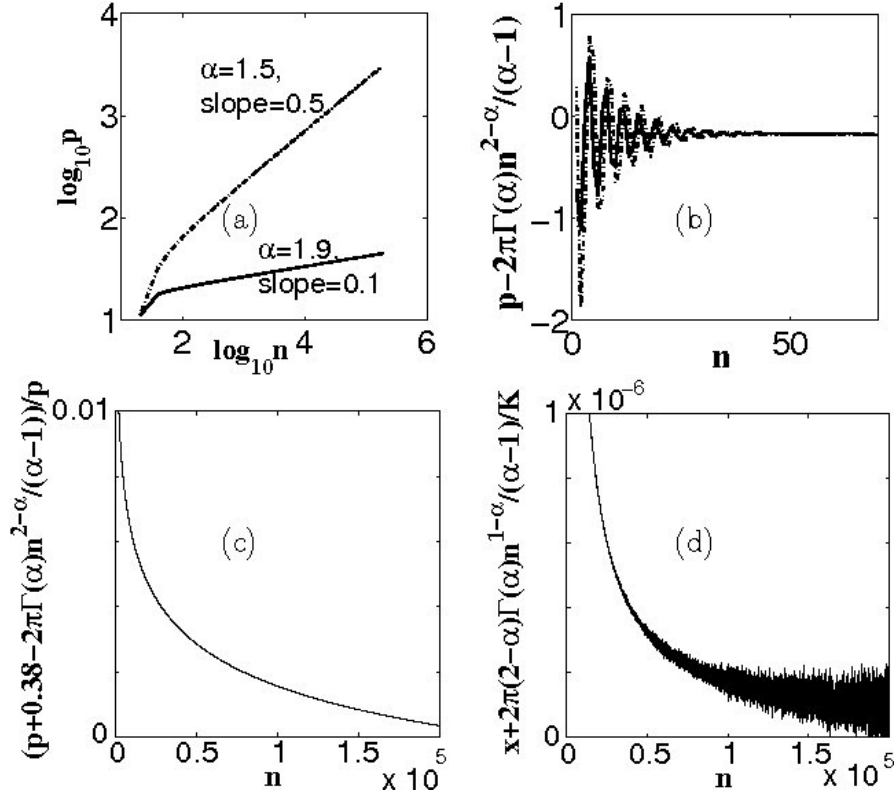


Fig. 14 Evaluation of the behavior of the attracting slow diverging trajectories: (a). Momenta for two trajectories with $x_n \approx 2\pi n$ in unbounded space (in this example $K = 2$). The solid line is related to a trajectory with $\alpha = 1.9$ and its slope is 0.1. The dashed line corresponds to a trajectory with $\alpha = 1.5$ and its slope is 0.5. (b). Deviation of momenta from the asymptotic formula for two trajectories with $x_n \approx 2\pi n$ in unbounded space, $\alpha = 1.9$, and $K = 2$. The dashed line has $p_0 = 7$ and the solid one $p_0 = 6$. (c). Relative deviation of the momenta for the trajectories in (b) from the asymptotic formula. (d). Deviation of the x -coordinates for the trajectories in (b) from the asymptotic formula.

the deviation from the asymptotic formula Eq. (95) and the relative difference with respect to Eq. (95).

As for $K < K_{c1}$, in the case $K_{c1}(\alpha) < K < K_{c2}(\alpha)$ asymptotic existence and stability of the antisymmetric sink (Sec. 3.3.1) is a result of the gradual transformation of the standard map's elliptic point with the decrease in the order of derivative from $\alpha = 2$ (see Fig. 15). Convergence of trajectories follows Eqs. (89)-(91).

The standard map's antisymmetric $T = 2$ trajectory becomes unstable when $K = 2\pi$ and at the point $(\pi/2, 0)$ in phase space a pair of $T = 2$ trajectories with $x_{n+1} = x_n - \pi$, $p_{n+1} = -p_n$ appears. Numerical simulations of the fractional standard maps (see Fig. 16) show that they demonstrate similar behavior. With the assumption that the RL-standard map Eqs. (61) and (62) have an asymptotic solution

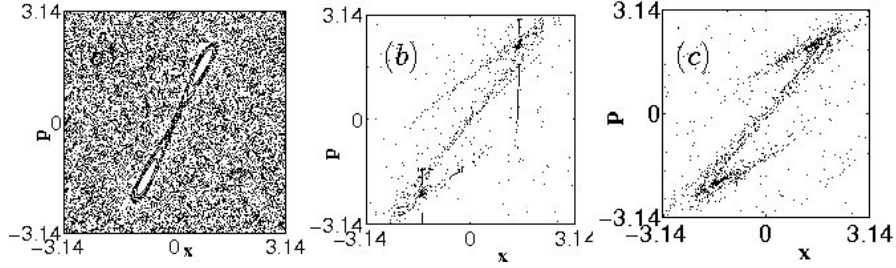


Fig. 15 Stable antisymmetric $x_{n+1} = -x_n$, $p_{n+1} = -p_n$ period $T = 2$ trajectories for $K = 4.5$: (a). 1000 iterations on each of 25 trajectories for the standard map with $K = 4.5$. The only feature is a system of two islands associated with the period two elliptic point. (b). RL-standard map stable $T = 2$ antisymmetric sink for $\alpha = 1.8$. 500 iterations on each of 25 trajectories: $p_0 = 0.0001 + 0.08i$, $0 \leq i < 25$. Slow and fast converging trajectories. (c). Caputo-standard map stable $T = 2$ antisymmetric sink for $\alpha = 1.8$. 1000 iterations on each of 10 trajectories: $p_0 = -3.1415 + 0.628i$, $0 \leq i < 10$.

$$p_n = (-1)^n p_l, \quad x_n = x_l - \frac{\pi}{2} [1 - (-1)^n] \quad (96)$$

it can be shown from Eq. (61) that the relationship $p_l = K/2 \sin(x_l)$ (Eq. (71)) is valid in this case too.

Numerical simulations similar to those presented in Fig. 13 show that for $K > K_{c2}$ (see Fig. 9) the RL-standard map has the asymptotic behavior

$$p_n = (-1)^n p_l + A n^{1-\alpha}, \quad (97)$$

where A is the same for both even and odd values of n . After substituting (97) in

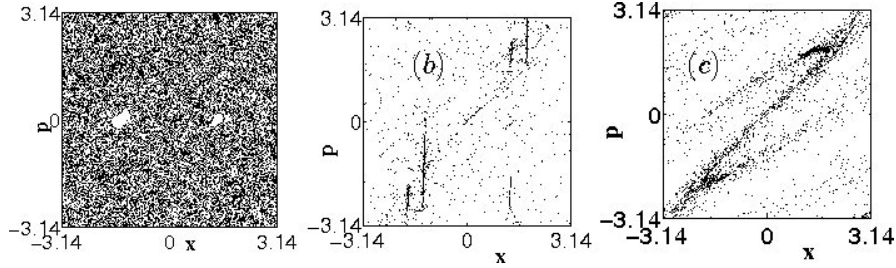


Fig. 16 Stable $x_{n+1} = x_n - \pi$, $p_{n+1} = -p_n$ period $T = 2$ trajectories for $K > K_{c2}$: (a). 500 iterations on each of 50 trajectories for the standard map with $K = 6.4$. The main features are two accelerator mode sticky islands around points $(-1.379, 0)$ and $(1.379, 0)$ which define the dynamics. Additional features - dark spots at the top and the bottom of the figure (which are clear on a zoom) - two systems of $T = 2$ tiny islands associated with two $T = 2$ elliptic points: $(1.379, \pi)$, $(1.379 - \pi, -\pi)$ and $(\pi - 1.379, \pi)$, $(-1.379, -\pi)$. (b). Two RL-standard map's stable $T = 2$ sinks for $K = 4.5$, $\alpha = 1.71$. 500 iterations on each of 25 trajectories: $p_0 = 0.0001 + 0.08i$, $0 \leq i < 25$. (c). Two Caputo-standard map's stable $T = 2$ sinks for $K = 4.5$, $\alpha = 1.71$. 1000 iterations on each of 10 trajectories: $p_0 = -3.1415 + 0.628i$, $0 \leq i < 10$.

(62) in the limit $n \rightarrow \infty$ one can derive

$$\sin(x_l) = \frac{\pi\Gamma(\alpha)}{KV_{\alpha l}}, \quad (98)$$

which has solutions when

$$K > K_{c2} = \frac{\pi\Gamma(\alpha)}{V_{\alpha l}} \quad (99)$$

(see Fig. 9). The value of A can also be calculated:

$$A = \frac{2x_l - \pi}{2\Gamma(2 - \alpha)}. \quad (100)$$

Results of the analytic estimations Eqs. (98) -(100) are in good agreement with the direct numerical simulations of the fractional standard maps.

3.3.4 Cascade of Bifurcations Band

At $K \approx 6.59$ in the standard map $T = 2$ points become unstable and stable $T = 4$ elliptic points appear. Further increase in K results in the period doubling cascade of bifurcations which leads to the disappearance of the corresponding islands of stability in the chaotic sea at $K \approx 6.6344$ (see Sec. 3.1.2). The cusp in Fig. 9(a) points to a point $\alpha = 2$ and $6.59 < K_* < 6.63$. Inside the band leading to the cusp a new type of attractors, cascade of bifurcations type trajectories (CBTT), appears (see Fig. 17). The lower boundary of the band approximately corresponds to the transition from the $T = 2$ sink $x_{n+1} = x_n - \pi$, $p_{n+1} = -p_n$ to the $T = 4$ sink and the upper boundary corresponds to the transition to chaos. At $\alpha = 1$ the lower and upper boundaries correspond to the $T = 2 \rightarrow T = 4$ transition and the transition to chaos in the 1D standard map (see Sec. 3.1.1). In CBTT period doubling cascade of bifurcations occurs on a single trajectory with a fixed value of the map parameter. A typical CBTT's behavior is similar to the behavior of trajectories in Hamiltonian dynamics in the presence of sticky islands: occasionally a trajectory enters a CBTT and then leaves it and enters the chaotic sea (Figs. 17 (a) and (b)). With the decreases in α the relative time trajectories spend in CBTT increases. CBTT are barely distinguishable near the cusp (Fig. 17(c)) and trajectories spend relatively little time in CBTT. A trajectory enters a CBTT after a few iterations and stays there over the longest computational time we were running our codes - 500000 iterations when α is close to one.

The CBTT in Fig. 17 were obtained for the RL-standard map. In many cases it is difficult to find CBTT in phase space of the Caputo-standard map but they look almost the same for both fractional maps on the x vs. n plot (see Fig. 17(b)).

Results of numerical simulations submitted for publication show that not CBTT but inverse (in time) CBTT, are present within the CBTT band (from the $T = 2 \rightarrow T = 4$ transition to the transition to chaos) of the fractional logistic maps.

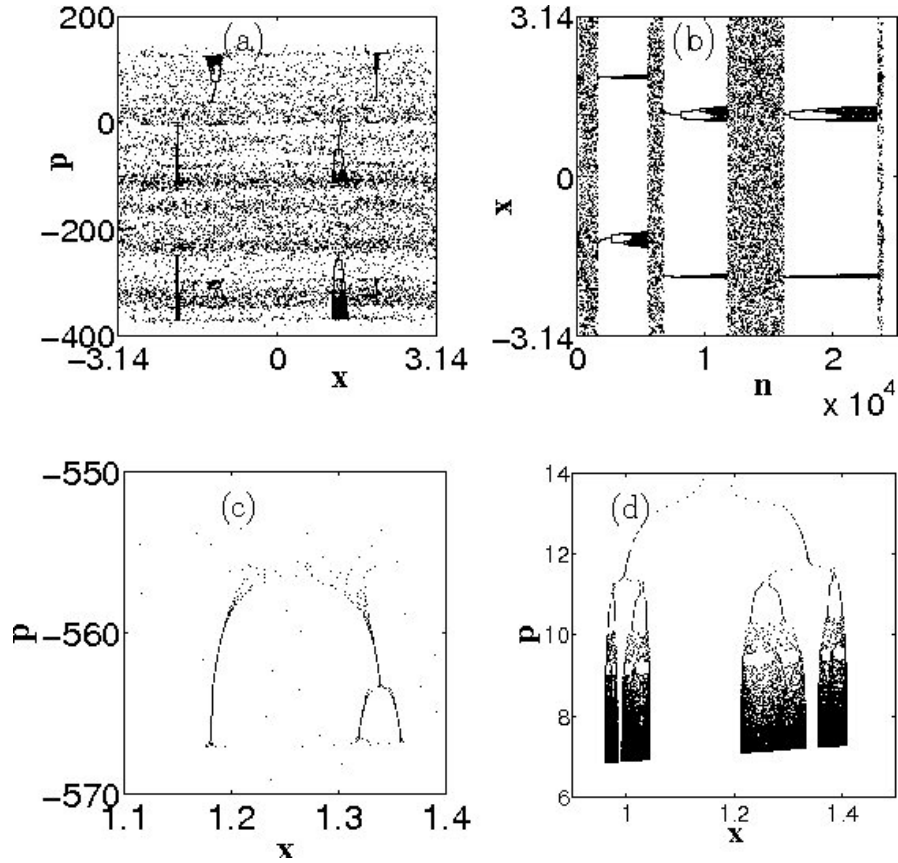


Fig. 17 Cascade of bifurcations type trajectories in the RL-standard map: (a). $\alpha = 1.65, K = 4.5$; one intermittent trajectory in phase space. (b). Time dependence of the coordinate x (x of n) for the case (a). (c). $\alpha = 1.98, K = 6.46$; zoom of a small feature for a single intermittent trajectory in phase space. (d). $\alpha = 1.1, K = 3.5$; a single trajectory enters the cascade after a few iterations and stays there during 500000 iterations.

3.3.5 More Fractional Attractors

In the one-dimensional standard map with $K > 0$ the “proper” chaotic attractor exists for $3.532 < K < 4.603339$ (see Sec. 3.1.1). This is the interval between the upper boundary of the CBTT band for $\alpha = 1$ and $K = K_{c3}(1)$ in Fig. 9. In the area between $K = K_{c3}(\alpha)$ curve and the upper border of the CBTT band (in Fig. 9) the fractional chaotic attractors are proper (see Fig. 18(a)) and above $K = K_{c3}(\alpha)$ the entire phase space is chaotic (Fig. 18(b)).

The standard map has a set of bands for K above $2\pi n$ of the accelerator mode sticky islands in which momentum increases proportionally to the number of iterations n and coordinate increases as n^2 (see Sec. 3.1.2). In the one-dimensional

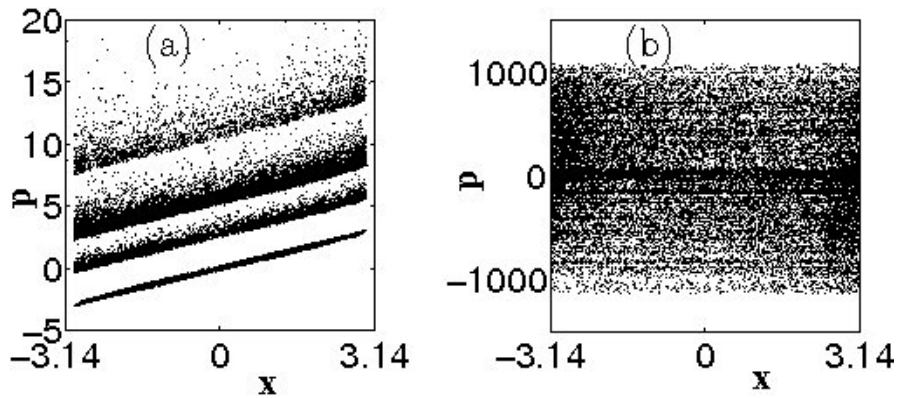


Fig. 18 “Proper” and “improper” attractors in the RL-standard map. 3000 iterations on ten trajectories with the initial conditions $x_0 = 0$, $p_0 = 0.001 + 1.65i$, $i = 0, 1, \dots, 9$: (a). A “proper” chaotic attractor for $K = 4.2$, $\alpha = 1.1$. (b). An “improper” chaotic attractor for $K = 4.4$, $\alpha = 1.1$.

standard map the corresponding bands demonstrate cascades of bifurcations (see Fig. 9(b)) for $|K|$ above $2\pi|n|$. The acceleration in those bands is zero and x increases proportionally to n (see Sec. 3.1.1).

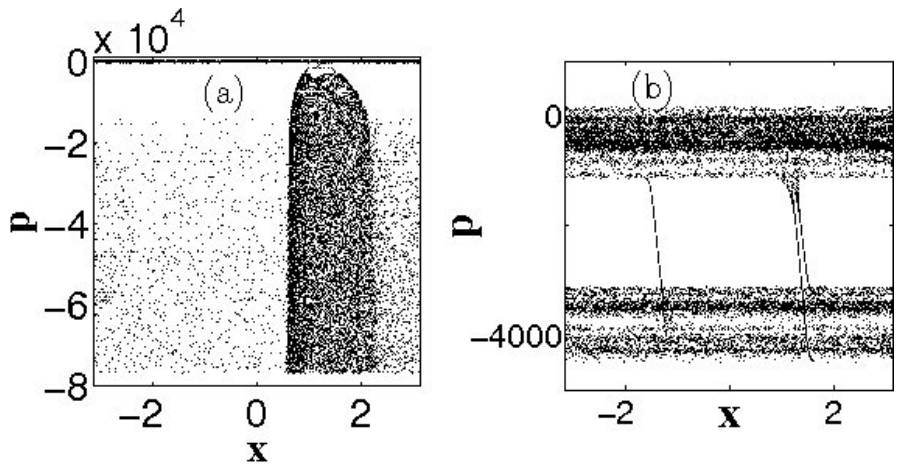


Fig. 19 RL-standard map’s accelerator mode attractors. 25000 iterations on a single trajectory with the initial conditions $x_0 = 0$, $p_0 = 0.1$: (a). CBTT-type accelerator mode attractor for $K = 5.7$, $\alpha = 1.03$. (b). Accelerator mode attractor for $K = 7.6$, $\alpha = 1.97$.

Accelerator mode attractors in the case $1 < \alpha < 2$ are not fully investigated. The standard map’s accelerator mode islands evolve into the accelerator mode (ballistic) attracting sticky trajectories when α is reduced from 2 for the values of K which increase with the decrease in α (Fig. 19(b)). When the value of α increases from

1, the corresponding ballistic attractors evolve into the cascade of bifurcation type ballistic trajectories (see Fig. 19(a)) for the values of K which decrease with the increase in α . This could mean that corresponding features in the one- and two-dimensional maps (at least for $K = 2\pi$) are not connected by the continuous change in α .

3.4 α -Families of Maps ($2 < \alpha < 3$)

Fractional maps for $\alpha > 2$ are not yet investigated. Here we'll present the first results [20] for the RL-standard map.

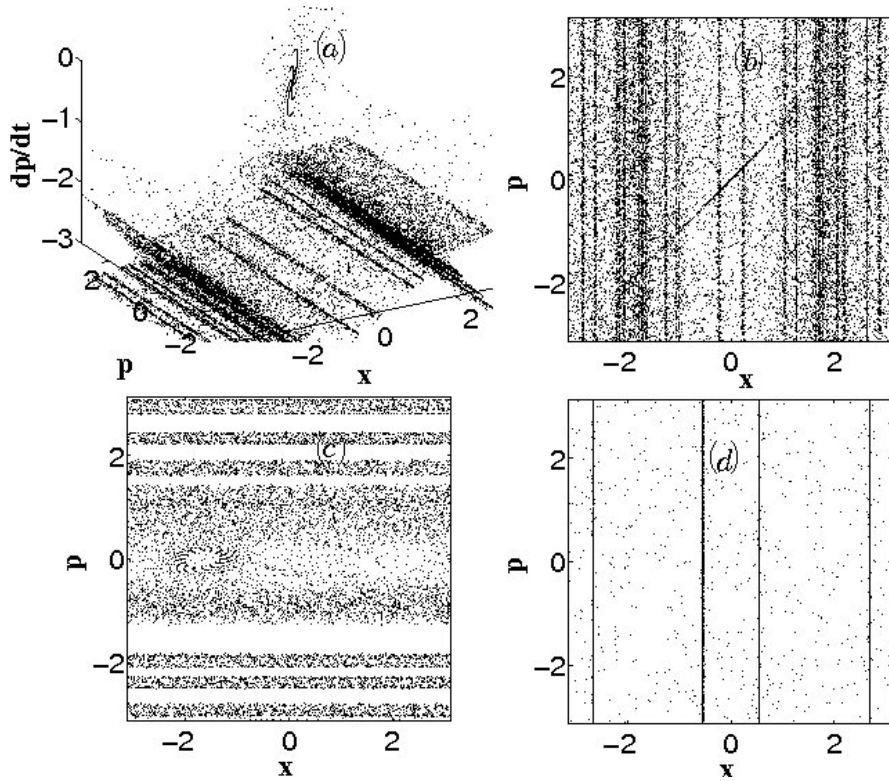


Fig. 20 RL-standard map for $2 < \alpha < 3$: (a). 3D phase space for $K = 1$, $\alpha = 2.01$ obtained on a single trajectory with $x_0 = p_0 = 0$ and $p_0^1 = 0.01$. (b). Projection of the phase space in (a) on the x - y plane. (c). Projection of the phase space for $K = 0.2$, $\alpha = 2.01$, $x_0 = p_0 = 0$ on the x - y plane obtained using 20 trajectories with different initial values of p_0^1 . (d). The same as in (c), but for $K = 4$ and $\alpha = 2.9$.

With $G_K(x) = K \sin(x)$ in Eqs. (36) and (37), the RL-standard map for $2 < \alpha \leq 3$ can be written as

$$\begin{aligned} p_{n+1}^1 &= p_n^1 - K \sin(x_n), \\ p_{n+1} &= p_n^1 + p_n - K \sin(x_n), \pmod{2\pi}, \\ x_{n+1} &= \frac{p_0}{\Gamma(\alpha-1)}(n+1)^{\alpha-2} + \frac{1}{\Gamma(\alpha)} \sum_{k=0}^n p_{k+1}^1 V_\alpha^1(n-k+1), \pmod{2\pi}. \end{aligned} \quad (101)$$

In our simulations we did not find a stable fixed point even for small values of K (see Fig. 20 (c)). Simulations show that for this map there are attractors in the form of the attracting multi-period lines with constant x (see Fig. 20 (a), (b), and (d)). For most of the values of the map parameters the phase space is highly chaotic.

This case and the transition from the 2D standard map to the 3D standard map is not yet fully investigated.

4 Conclusion

The systems with long-term memory that are most frequently encountered in nature are systems with power-law memory. In many applications, including biological applications, the exponent in power law, $\sim t^{-\beta}$, is $0 < \beta < 1$. This is true, in particular, for adaptive systems and for viscoelastic properties of human tissues. These systems can be described by nonlinear fractional differential equations with fractional derivatives of the order $\alpha = 1 - \beta$ with $0 < \alpha < 1$. Fractional differential equations can be modeled by discrete nonlinear maps with power-law memory. We studied maps which model fractional differential equations with $0 < \alpha < 2$ and, correspondingly, $-1 < \beta < 1$. Decrease in β and, correspondingly, increase in α means an increase in the memory effects - older states have higher weights in the definition of the present state of a system.

In Sec. 3 we showed that an increase in memory effects leads to more complicated and chaotic behavior. As can be seen in Fig. 6, systems with small α are more stable. At the values of system parameters, corresponding to the periodic behavior and transition to chaos, behavior of such systems follows a well defined cascade of bifurcations pattern Fig. 7. This type of evolution may mean a slow adaptation when a system changes its state long after a change in a parameter occurred.

Increase in memory effects with the transition from $0 < \alpha < 1$ to $1 < \alpha < 2$ leads to increased diversity in systems' behavior. Systems with $1 < \alpha < 2$ may demonstrate periodic sinks, attracting slow diverging trajectories, attracting accelerator mode trajectories, chaotic attractors, and cascade of bifurcations and inverse cascade of bifurcations type attracting trajectories. An intermittent cascade of bifurcations type behavior (Figs. 17 (a) and (b)) may correspond to a scenario of the evolution of chronic diseases, to some mental disorders, or to the evolution of some social systems.

The way in which systems with power-law memory approach fixed and periodic points (Eqs. (89)-(91)) can be used to identify systems with memory in an analysis of experimental data.

Acknowledgments

The author expresses his gratitude to V. E. Tarasov for useful discussions, to E. Hameiri and H. Weitzner for the opportunity to complete this work at the Courant Institute, and to V. Donnelly for technical help.

References

1. Anderson, J.R., 1995, *Learning and memory: An integrated approach*, Wiley, New York.
2. Arrowsmith, D.K. and Place, C.M., 1990, *An introduction to dynamical systems*, Cambridge University Press, Cambridge.
3. Ausloos, A. and Dirickx, M. (Eds), 2006, *The Logistic Map and the Route to Chaos*, Springer, Berlin, Heidelberg, New York.
4. Bagley, R.L. and Torvik, P.J., 1983a, A Theoretical Basis for the Application of Fractional Calculus to Viscoelasticity, *Journal of Rheology*, **27**, 201–210.
5. Bagley, R.L. and Torvik, P.J., 1983b, Fractional Calculus - A Different Approach to the Analysis of Viscoelastically Damped Structures, *AIAA Journal*, **21**, 741–748.
6. Brauer, F. and Castillo-Chavez, C., 2001, *Mathematical Models in Population Biology and Epidemiology*, Springer, New York.
7. Caponetto, R., Dongola, G., Fortuna, L., and Petras, I., 2010, *Fractional Order Systems: Modeling and Control Applications*, World Scientific, Singapore.
8. Caputo M. and Mainardi, F., 1971a, A new dissipation model based on memory mechanism, *Pure and Applied Geophysics*, **91**, 134–147.
9. Caputo M. and Mainardi, F., 1971b, Linear models of dissipation in anelastic solids, *Rivista del Nuovo Cimento*, **1**, 161–198.
10. Cheng, S., Clarke, E.C., and Bilston, L.E., 2008, Rheological properties of the tissues of the central nervous system: A review, *Medical Engineering and Physics*, **30**, 1318–1337.
11. Chirikov, B.V., 1979, A universal instability of many dimensional oscillator systems, *Physic Reports*, **52**, 263–379.
12. Coussot, C., Kalyanam, S., Yapp, R., and Insana, M.F., 2009, Fractional Derivative Models for Ultrasonic Characterization of Polymer and Breast Tissue Viscoelasticity, *IEEE Transactions on Ultrasonics, Ferroelectrics and Frequency Control*, **56**, 715–726.
13. Craiem, D.O. and Armentano, R.L., 2006, Arterial viscoelasticity: a fractional derivative model, *Engineering in Medicine and Biology Society, EMBS '06. 28th Annual International Conference of the IEEE*, 1098–1101.
14. Craiem, D.O., Rojo, F.J., Atienza, J.M., Guinea, G.V., and Armentano, R.L., 2006, Fractional calculus applied to model arterial viscoelasticity, *Latin American Applied Research*, **38**, 141–145.
15. Cvitanovic, P., 1989, *Universality in chaos*, Adam Hilger, Bristol.
16. Doehring, T.C., Freed, A.D., Carew, E.O., and Vesely, I., 2005, Fractional order viscoelasticity of the aortic valve cusp: An alternative to quasilinear viscoelasticity, *Journal of Biomechanical Engineering*, **127**, 700–708.
17. Duck, F.A., 1990, *Physical Properties of Tissue: A Comprehensive Reference Book*, Academic Press, San Diego.

18. Dullin, H.R. and Meiss, J.D., 2012, Resonances and Twist in Volume-Preserving Maps, *SIAM Journal on Applied Dynamical Systems*, **11**, 319–359.
19. Edelman, M., 2011, Fractional Standard Map: Riemann-Liouville vs. Caputo, *Communications in Nonlinear Science and Numerical Simulation*, **16**, 4573–4580.
20. Edelman, M., 2013, Fractional Maps and Fractional Attractors. Part I: α -Families of Maps, Discontinuity, Nonlinearity, and Complexity, **1**, 305–324.
21. Edelman, M. and Taieb, L.A., 2013, New types of solutions of non-linear fractional differential equations, in: *Advances in Harmonic Analysis and Operator Theory*; Series: *Operator Theory: Advances and Applications*, Eds: Almeida, A., Castro, L., and F.-O. Speck, F.-O., **229**, 139–155, Springer, Basel.
22. Edelman, M. and Tarasov, V.E., 2009, Fractional standard map, *Physica Letters A*, **374**, 279–285.
23. Fairhall, A.L., Lewen, G.D., Bialek, W., and de Ruyter van Steveninck, R.R., 2001, Efficiency and Ambiguity in an Adaptive Neural Code, *Nature*, **412**, 787–792.
24. Feigenbaum, M., 1978, Quantitative Universality for a Class of Non-Linear Transformations, *Journal of Statistical Physics*, **19**, 25–52.
25. Feller, W., 1968, *An introduction to probability theory and its applications*, Wiley, New York.
26. Fick, E., Fick, M., and Hausmann, G. 1991, Logistic equation with memory, *Physical Review A*, **44**, 2469–73.
27. Fulinski, A. and Kleczkowski A.S., 1987, Nonlinear maps with memory, *Physica Scripta*, **335**, 119–122.
28. Gallas, J.A.C., 1993a, Simulating memory effects with discrete dynamical systems, *Physica A*, **195**, 417–430.
29. Gallas J.A.C., 1993b, Simulating memory effects with discrete dynamical systems, *Physica A*, **198**, 339–339 (erratum).
30. Giona, M., 1991, Dynamics and relaxation properties of complex systems with memory, *Nonlinearity*, **4**, 911–925.
31. Grahovac, N.M. and Zigic, M.M., 2010, Modelling of the hamstring muscle group by use of fractional derivatives, *Computers and Mathematics with Applications*, **59**, 1695–1700.
32. Hartwich, K. and Fick, E., 1993, Hopf bifurcations in the logistic map with oscillating memory, *Physica Letters A*, **177**, 305–310.
33. Hénon, M., 1969, Numerical study of quadratic area-preserving mappings, *Quarterly of Applied Mathematics*, **XXVII**, 291–312.
34. Holm, S. and Sinkus, R., 2010, A unifying fractional wave equation for compressional and shear waves, *Journal of the Acoustical Society of America*, **127**, 542–548.
35. Hoppensteadt, F., 1975, *Mathematical Theories of Populations: Demographics, Genetics, and Epidemics*, SIAM, Philadelphia.
36. Hoyt, K., Castaneda, B., Zhang, M., Nigwekar, P., di SantAgnese, A., Joseph, J.V., Strang, J., Rubens, D.J., and Parker, K.J., 2008, Tissue elasticity properties as biomarkers for prostate cancer *Cancer Biomarkers*, **4**, 213–225.
37. Kahana, M.J., 2012, *Foundations of human memory*, Oxford University Press, New York.
38. Kilbas, A.A., Bonilla, B., and Trujillo, J.J., 2000a, Nonlinear differential equations of fractional order is space of integrable functions, *Doklady Mathematics*, **62**, 222–226.
39. Kilbas, A.A., Bonilla, B., and Trujillo, J.J., 2000b, Existence and uniqueness theorems for nonlinear fractional differential equations, *Demonstratio Mathematica*, **33**, 583–602.
40. Kilbas, A.A., Srivastava, H.M., and Trujillo, J.J., 2006, *Theory and Application of Fractional Differential Equations*, Elsevier, Amsterdam.
41. Kobayashi, Y., Watanabe, H., Hoshi, T., Kawamura, K., and Fujie, M.G., 2012, Viscoelastic and Nonlinear Liver Modeling for Needle Insertion Simulation, *Soft Tissue Biomechanical Modeling for Computer Assisted Surgery*, *Studies in Mechanobiology, Tissue Engineering and Biomaterials*, **11**, 41–67.
42. Landford, O.E., 1982, A Computer-Assisted Proof of the Feigenbaum Conjectures, *Bulletin of the American Mathematical Society*, **6**, 427–434.

43. Leopold, D.A., Murayama, Y., and Logothetis, N.K., 2003, Very slow activity fluctuations in monkey visual cortex: implications for functional brain imaging, *Cerebral Cortex*, **13**, 422–433.
44. Libertiaux, V. and Pascon, F., 2010, Differential versus integral formulation of fractional hyperviscoelastic constitutive laws for brain tissue modeling, *Journal of Computational and Applied Mathematics*, **234**, 2029–2035.
45. Lichtenberg, A.J. and Leiberman, M.A., 1992, *Regular and Chaotic Dynamics*, Springer, Berlin.
46. Lomeli, H.E. and Meiss, J.D., 1998, Quadratic volume-preserving maps, *Nonlinearity*, **11**, 557–574.
47. Lundstrom, B.N., Higgs, M.H., Spain, W.J., and Fairhall, A.L., 2008, Fractional differentiation by neocortical pyramidal neurons, *Nature Neuroscience*, **11**, 1335–1342.
48. Lundstrom, B.N., Fairhall, A.L., and Maravall, M., 2010, Multiple time scale encoding of slowly varying whisker stimulus envelope in cortical and thalamic neurons in vivo, *The Journal of Neuroscience*, **30**, 5071–5077.
49. Mace, E., Cohen, I., Montaldo, G., Miles, R., 2011, In Vivo Mapping of Brain Elasticity in Small Animals Using Shear Wave Imaging, *IEEE Transactions on Medical Imaging*, **30**, 550–558.
50. Magin, R. L., 2010, Fractional calculus models of complex dynamics in biological tissues, *Journal of Computational and Applied Mathematics*, **59**, 1586–1593.
51. Mainardi, F., 1994, Fractional relaxation in anelastic solids. *Journal of Alloys and Compounds*, **211**, 534–538.
52. Mainardi, F., 2010, *Fractional Calculus and Waves in Linear Viscoelasticity: An Introduction to Mathematical Models*, Imperial College Press, London.
53. Mainardi, F., 2012, An historical perspective on fractional calculus in linear viscoelasticity, *Fractional Calculus and Applied Analysis*, **15**, 712–717.
54. Mainardi, F. and Gorenflo, R., 2007, Time fractional derivatives in relaxation processes: a tutorial survey, *Fractional Calculus and Applied Analysis*, **10**, 269–308.
55. Mariappan, Y.K., Glaser, K.J., and Ehman, R.L., 2010, Magnetic Resonance Elastography: A Review, *Clinical Anatomy*, **23**, 497–511.
56. May, R.M., 1976, Simple mathematical models with very complicated dynamics, *Nature*, **261**, 459–467.
57. Min, W., Luo, G., Cherayil, B.J., Kou, S.C., and Xie, X.S., 2005, Observation of a power-law memory kernel for fluctuations within a single protein molecule, *Physical Review Letters*, **94**, 198302.
58. Moser, J., 1994, On quadratic symplectic mappings, *Mathematische Zeitschrift*, **216**, 417–430.
59. Nasholm, S.P. and Holm, S., 2013, On a Fractional Zener Elastic Wave Equation, *Fractional Calculus and Applied Analysis*, **16**, 26–50.
60. Nicolle, S., Vezin, P., and Palierna, J.-F., 2010, A strain-hardening bi-power law for the non-linear behaviour of biological soft tissues, *Journal of Biomechanics*, **43**, 927–932.
61. Nicolle, S., Noguera, L., Palierna, J.-F., 2012, Shear mechanical properties of the spleen: Experiment and analytical modelling, *Journal of the Mechanical Behavior of Biomedical Materials*, **9**, 130–136.
62. Petras, I., 2011, *Fractional-Order Nonlinear Systems*, Springer, Heidelberg.
63. Podlubny, I., 1999, *Fractional Differential Equations*, Academic Press, San Diego.
64. Prieur, F. and Holm, S., 2011, Nonlinear acoustic wave equations with fractional loss operators. *Journal of the Acoustical Society of America*, **130**, 1125–1132.
65. Prieur, F., Vilenskiy, G., and Holm, S., 2012, A more fundamental approach to the derivation of nonlinear acoustic wave equations with fractional loss operators, *Journal of the Acoustical Society of America*, **132**, 2169–2172.
66. Rubin, D.C. and Wenzel, A.E., 1996, One Hundred Years of Forgetting: A Quantitative Description of Retention, *Psychological Review*, **103**, 743–760.
67. Samko, S.G., Kilbas, A.A., and Marichev, O.I., 1993, *Fractional Integrals and Derivatives Theory and Applications*, Gordon and Breach, New York.

68. Schmidt, G., 1980, Stochasticity and fixed-point transitions, *Physical Review A*, **22**, 2849–2854.
69. Sommacal, L., Melchior, P., Oustaloup, A., Cabelguen, J.-M., and Ijspeert, A.J., 2008, Fractional Multi-model of the Frog Gastrocnemius Muscle, *Journal of Vibration and Control*, **14**, 1415–1430.
70. Stanislavsky, A.A., 2006, Long-term memory contribution as applied to the motion of discrete dynamical system, *Chaos*, **16**, 043105.
71. Szabo, T.L. and Wu, J., 2000, A model for longitudinal and shear wave propagation in viscoelastic media, *Journal of the Acoustical Society of America*, **107**, 2437–2446.
72. Takeuchi, Y., Iwasa, Y., and Sato K. (Eds), 2007, *Mathematics for Life Science and Medicine*, Springer, Berlin, Heidelberg, New York.
73. Tarasov, V.E., 2008a, Fractional equations of Curie-von Schweidler and Gauss laws, *Journal of Physics: Condensed Matter*, **20**, 145212.
74. Tarasov, V.E., 2008b, Universal electromagnetic waves in dielectrics, *Journal of Physics: Condensed Matter*, **20**, 175223.
75. Tarasov, V.E., 2009a, Differential equations with fractional derivative and universal map with memory, *Journal of Physics A: Mathematical and Theoretical*, **42**, 465102.
76. Tarasov, V.E., 2009b, Discrete map with memory from fractional differential equation of arbitrary positive order, *Journal of Mathematical Physics*, **50**, 122703.
77. Tarasov, V.E., 2009c, Fractional integro-differential equations for electromagnetic waves in dielectric media, *Theoretical and Mathematical Physics*, **158**, 355–359.
78. Tarasov, V.E., 2011, *Fractional Dynamics: Application of Fractional Calculus to Dynamics of Particles, Fields, and Media*, Springer, HEP, New York.
79. Tarasov, V.E. and Edelman, M., 2010, Fractional dissipative standard map, *Chaos*, **20**, 023127.
80. Tarasov, V.E. and Zaslavsky, G.M., 2008, Fractional equations of kicked systems and discrete maps, *Journal of Physics A: Mathematical and Theoretical*, **41**, 435101.
81. Taylor, L.S., Lerner, A.L., Rubens, D.J., and Parker, K.J., 2002, A Kelvin-Voigt Fractional Derivative Model for Viscoelastic Characterization of Liver Tissue, In: Scott, E.P, editor, *ASME International Mechanical Engineering Congress and Exposition*, LA, New Orleans.
82. Toib, A., Lyakhov, V., and Marom, S., 1998, Interaction between duration of activity and recovery from slow inactivation in mammalian brain Na⁺ channels, *Journal of Neuroscience*, **18**, 1893–1903.
83. Ulanovsky, N., Las, L., Farkas, D., and Nelken, I., 2004, Multiple time scales of adaptation in auditory cortex neurons, *Journal of Neuroscience*, **24**, 10440–10453.
84. Vul, E.B., Sinai, Y.G., and Khanin, K.M., 1984, Feigenbaum universality and the thermodynamic formalism, *Russian Mathematical Surveys*, **39**, 1–40.
85. Wineman, A., 2007, Nonlinear viscoelastic membranes, *Computers and Mathematics with Applications*, **53**, 168–181.
86. Wineman, A., 2009, Nonlinear Viscoelastic Solids - A Review, *Mathematics and Mechanics of Solids*, **14**, 300–366.
87. Wixted, J.T., 1990, Analyzing the empirical course of forgetting, *Journal of Experimental Psychology: Learning, Memory, and Cognition*, **16**, 927–935.
88. Wixted, J.T. and Ebbesen, E., 1991, On the form of forgetting, *Psychological Science*, **2**, 409–415.
89. Wixted, J.T. and Ebbesen, E., 1997, Genuine power curves in forgetting, *Memory & Cognition*, **25**, 731–739.
90. Zaslavsky, G.M., 2008, *Hamiltonian Chaos and Fractional Dynamics*, Oxford University Press, Oxford.
91. Zaslavsky, G.M. and Edelman, M., 2000, Hierarchical structures in the phase space and fractional kinetics: I. Classical systems, *Chaos*, **10**, 135–146.
92. Zaslavsky, G.M. and Edelman, M., 2004, Fractional kinetics: From pseudochaotic dynamics to Maxwell's Demon, *Physica D*, **193**, 128–147.
93. Zaslavsky, G.M., Edelman, M., and Niyazov, B.A., 1997, Self-Similarity, Renormalization, and Phase Space Nonuniformity of Hamiltonian Chaotic Dynamics, *Chaos*, **7**, 159–181.

94. Zeraoulia, E. and Sprott, J.C., 2010, *2-D Quadratic Maps and 3-D ODE Systems: A Rigorous Approach*, World Scientific, Singapore.
95. Zhang, M., Nigwekar, P., Castaneda, B., Hoyt, K., Joseph, J.V., di SantAgnese, A., Messing, E.M., Strang, J., Rubens, D.J., and Parker, K.J., 2008, Quantitative characterization of viscoelastic properties of human prostate correlated with histology, *Ultrasound in Medicine and Biology*, **34**, 1033-1042.
96. Zilany, M.S., Bruce, I.C., Nelson, P.C., and Carney, L.H., 2009, A phenomenological model of the synapse between the inner hair cell and auditory nerve: long-term adaptation with power-law dynamics, *Journal of the Acoustical Society of America*, **126**, 2390–2412.